

LAPPEENRANTA UNIVERSITY OF TECHNOLOGY

School of Engineering Science

Degree Programme in Technical Physics

Anum Rasheed

**Effect of humidity on electric potential of ZrO₂ nanocomposite investigated
by AFM/ KPFM**

Examiners: Professor Erkki Lähderanta

M.Sc. Pavel Geydt

ABSTRACT

LAPPEENRANTA UNIVERSITY OF TECHNOLOGY

School of Engineering Science

Degree Programme in Technical Physics

Anum Rasheed

Effect of humidity on electric potential of ZrO₂ nanocomposite investigated by AFM/KPFM

Master's thesis

2017

88 pages, 47 figures, 7 tables.

Examiners: Professor Erkki Lähderanta

M.Sc. Pavel Geydt

Keywords: ZrO₂, Hygroelectricity, nanocomposites, SPM, AFM, KPFM

ZrO₂ nanocomposites were investigated bearing in mind their potential in displaying varying surface potential due to changes in humidity in the environment. Scanning Probe Microscopy (SPM) was used in general for studying the electrical properties as it allowed the visualization of electrical properties. The sample was studied under different levels of humidity.

Kelvin Probe Force Microscopy (KPFM) was the main technique utilized to characterize the varying charge distribution on the sample's topography. The influence of humidity on the electric potential was shown. The results concluded that electrical potential changes with change in environment's humidity level.

ACKNOWLEDGEMENTS

Firstly, I would like to thank my professor, Erkki Lähderanta, for giving me the opportunity to be a part of this prestigious institute, Lappeenranta University of Technology, and his generous personality has been a source of inspiration throughout my course of study here.

I would like to thank late Tatyana Makarova, Andriy Lyubchick and Svitlana Lyubchick for initiating HUNTER Project Proposal “Advanced Humidity to Electricity Converter” which provided me an opportunity to carryout research in nanotechnology and write my Master’s thesis related to this research.

I would also like to thank my second supervisor, Pavel Geydt, for helping me put in writing this thesis and being there always to answer my queries.

Finally, I would like to thank my father for his encouragement to pursue my higher studies abroad, and my relatives and friends, especially Alekski Kervinen for his motivation during the writing of this thesis.

Lappeenranta, July 2017

Anum Rasheed

Table of Contents

1	Introduction	6
2	Literature Review	7
2.1	Water and electricity in historical perspective	8
2.2	Comparison of various energy producing techniques	9
2.2.1	Detailed Analysis of widely used renewable energy resources	12
2.2.2	Drawbacks of current electricity producing technologies	18
2.3	New alternative for electricity production	21
2.4	Electric potential at nanoscale.....	35
2.5	Recent studies of ZrO ₂ nanocomposite	37
3	Methodology.....	39
3.1	Scanning Probe Microscopy (SPM).....	40
3.2	Atomic Force Microscopy (AFM)	41
3.2.1	Kelvin Probe Force Microscopy (KPFM)	43
3.2.2	Quantitative Nanoscale Mechanical Property Mapping (QNM™)	48
4	Experimental Components and Procedure	50
4.1	Sensors	50
4.1.1	Working principle and type of Humidity Sensors	56
4.2	Soldering wires and connecting wires to mother board Arduino Uno.....	59
4.3	Software code.....	60
4.4	Setting variable environmental conditions.....	62
5	Measurements.....	66
6	Analysis of Results	73
	Summary	77
	References.....	80

List of Abbreviations

SPM	Scanning Probe Microscopy
AFM	Atomic Force Microscopy
STM	Scanning Tunneling Microscopy
KPFM	Kelvin Probe Force Microscopy
AM	Amplitude Modulation
FM	Frequency Modulation
CPD	Contact Potential Difference
LCPD	Local Contact Point Difference
F_{es}	Electrostatic force
QNM TM	Quantitative Nanoscale Mechanical Property Mapping
%RH	Percentage of Relative Humidity
RHIC	Relative Humidity Integrated Circuit
V_{SUPPLY}	Supply Voltage [V]
V_{OUT}	Output Voltage [V]
PV	Photovoltaics
E_g	Energy gap
Energy unit [EJ/yr]	Exajoule per year, (1EJ=1 x 10 ¹⁸ J)
EROEI	Energy Returned on Energy Invested
RHIC	Relative Humidity Integrated Circuit
RH	Relative Humidity
PVA	Polyvinyl-Alcohol

1 Introduction

Imagine a baby trapped in a sea covered in oil spills from a tank, or drinking water that contains mercury contaminants from a factory. Gasping for air because of the pollution surrounding him. This is a sad reality our next generation will face not in their adulthood but unlike us they will experience it the moment they open their eyes after being born. Most of the harmful environmental effects are a result of energy production and industrial processes that use non-renewable energy sources as fuels. A number of renewable energy resources are already in use at large scale but they are not compatible enough to shift all energy consuming processes to renewable energy source. Hence, there is a need to introduce more renewable energy sources. Inspired by Professor Richard Feynman's famous talk "There's plenty of room at the bottom", I was interested in conducting research at nanoscale and the opportunity was provided by Hunter's Project. The main goal was to find a suitable material that is porous in nature, absorbs moisture and is able to dissociate water into charges. Furthermore, the material should be able to buildup charge on its surface i.e. is capable of producing electric potential by capturing humidity which is known as Hygroelectricity. ZrO_2 was chosen to be studied as it was available and a suitable candidate because it is being produced in abundance as it has secured its place in multiple applications. No harmful or toxic substances are released during the manufacturing process.

Brief outline of each chapter is mentioned below to summarize the main content.

In chapter Literature Review, existing energy production methods have been analyzed thoroughly and their production methodologies, advantages and drawbacks have been discussed. This helped to conclude the need for an alternative source which is renewable, green, inexpensive and uses a source which is abundant.

In chapter Methodology Section, different classifications of SPM have been discussed with main emphasis on AFM, Peak Force QNMTM and KPFM. The main technique used to carry out the measurements was KPFM as it combined the AFM technique to construct a map of the topography and EFM that can measure the electric potential.

In the chapter, Experimental Components and Procedure, ZrO_2 is evaluated and the research that has already been conducted regarding ZrO_2 is discussed. Different sensors were considered in order to choose the reference humidity sensor and the final sensor to be used for the experiment are discussed in detail in the section Sensors. Arduino Uno was used to construct a stable experimental setup: how it was done and the code used to display the humidity readings on monitor are also discussed. Experimental setup and challenges faced during the establishment of the setup are also mentioned in detail. One important parameter of the experiment was to establish controlled humidity conditions which, are elaborately explained.

In the chapter Measurements, each reading is discussed separately and any abnormality that occurred for the readings is also discussed along with the procedures carried out to minimize it.

In the chapter, Analysis of Results, all the measurements carried out are analyzed as graph and the trend is discussed.

In Conclusions, the results obtained are combined as statements and in the Summary part, the purpose of this Master's Thesis is jotted down with recommendations for future studies and areas of improvement in the experiment that is carried out.

2 Literature Review

The modern lifestyle is in dire need of reliable and steady energy supply. We are dependent on energy from the moment we are born to the moment we die. However, energy should not be taken for granted and it is important to ensure that the energy production methods are not causing harm to the environment. Although most of the energy worldwide is produced using non-renewable energy resources, during 1980s intensive researches were carried out to highlight the risks factors associated with pollution caused by burning fossil fuels and stimulated research for renewable energy production methods [1].

Various renewable energy production techniques are being exploited to produce desired electrical energy, but they are not enough and have their limitations and drawbacks although not as severe as the non-renewable energy resources. This has led to the search for new cleaner and greener energy resources. One such technique, Hygroelectricity i.e. the production of electricity

due to humidity, is discussed in detail in this thesis. Earth's hydrosphere which means the total amount of water on Earth, consists of free water in solid, liquid or gaseous states on Earth's surface, atmosphere and deep inside the core to a depth of 2000 m. Approximately, hydrosphere of Earth contains 1,386 million cubic kilometers (km^3) water however, 97.5 percent of this free water is saline in nature whereas, only 2.5 percent is fresh water. 68.7 percent of this fresh water is in the Antarctic and mountainous regions in the form of permanent snow cover and ice [2]. The above mentioned approximate numerical figures are long-term average values. However, for shorter times intervals, amount of water in the hydrosphere changes due to exchange of water among land, oceans and the atmosphere and this exchange is usually referred as global hydrological cycle.

2.1 Water and electricity in historical perspective

“Age of water power” during the Middle ages (from 5th to 15th century) [3], proved to be a strong milestone, which initiated the beginning of harnessing energy from natural resources. European antiquity discovered the potential of moving water and many ways were developed, to harness energy from water which greatly improved the lifestyle of people as energy produced by moving water was utilized to carry out functions that were impossible to do with the muscular power of humans and animals. The origins of water-driven movers are ambiguous but, the first reference of their existence is associated with Antipater of Thessalonica during the first century [4], Water-wheel was an important invention because it was used in mills to carry out multiple functions such as tanning leather, grinding grains, saw wood and a variety of simple industrial processes [3]. The earliest wheels crafted were horizontal and the water was directed onto the wooden paddles through a trough made up of wood and inclined at a specific angle [4]. The paddles were fitted to a wooden shaft attached to a milling stone above as shown in Figure 1.

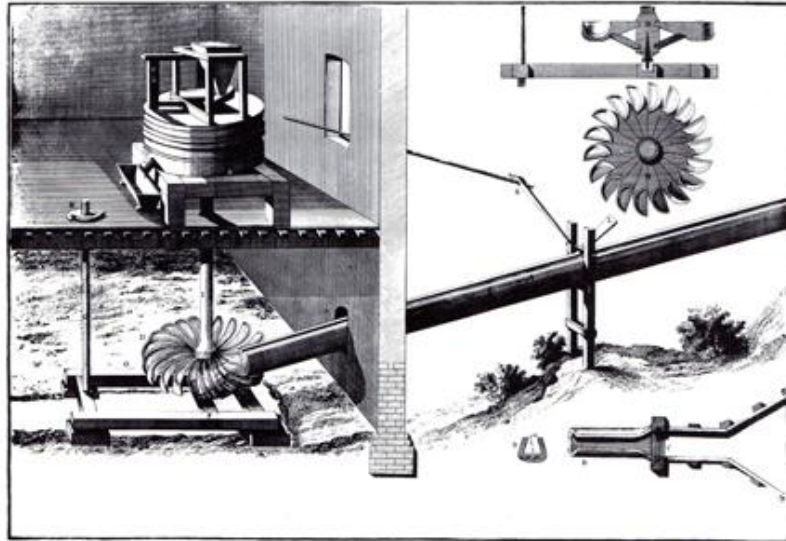


Figure 1: Diagrammatic representation of earliest horizontal water-powered mill [5].

Water energy quickly gained fame and was explored. It led to the creation of hydraulic machines. In the Middle Ages, mills were mounted on bridges and boats, giving birth to the idea of creation of dams to store water and built-up pressure in-order to use the potential energy of stored water. Moreover, water could also be diverted into multiple streams [4] and canals from which it was used to drive wheels and to carry out multiple tasks simultaneously.

2.2 Comparison of various energy producing techniques

The primary difference between renewable resources and fossil fuels is that renewable energy resources cannot be exhausted and enjoy zero or low economic value prior to being converted to valuable form. The only hindrance is the construction cost of the device for energy collection [6]. After the construction of the plant and when it is fully functional, those systems, which utilize non-renewable energy resources (for instance fossil fuels), convert only part of the utilized energy into a useful energy. On the other hand, systems that harness their energy from renewable energy resources transform available energy into useful one which adds on to the energy reserves, although at a lower rate [7]. However, the non-renewable energy systems use

fossil fuels, which contribute to total energy produced, but on the expense of the resource stock and the amount of energy used from the total produced energy is also smaller.

Table 1 provides a comparison of Energy Returned on Energy Invested (EROEI).

Table 1: Comparison of EROEI and price in Cents/kWh of various energy sources [7].

Energy mechanism	EROEI	Cents/kWh
Hydro	11:1 - 267:1	1
Coal	50:01	2- 4
Oil (global average)	19:01	-
Natural gas	10:01	4 - 7
Wind	18:01	4.5 - 10
Wave	15:01	12
Solar Photovoltaic	3.75:1 - 10:1	21 - 83
Geothermal	2:1 - 13:1	10
Tidal	~ 6:1	10
Nuclear	1.1:1 - 15:1	2 - 9
Biodiesel	1.9:1 - 9:1	
Solar thermal	1.6:1	6 - 15
Ethanol	0.5:1 - 8:1	-

EROEI= useful acquired energy / useful energy expended

Where “useful” means the energy that is available for use to humans. The higher the value of EROEI, the better the process is. When the value of EROEI goes below 1, more energy is utilized during the extraction process compared to the output energy available for use [7]. Although coal and oil have higher EROEI values, they are non-renewable energy sources. As visible from the table, renewable energy sources have low EROEI compared to coal and oil which signifies the importance of search for new renewable energy sources.

All the systems compared in the table have the same life span. Lifetime of systems utilizing renewable energy sources is greater than those systems which make use of fossil fuels. Renewable energy systems may either have a lower or greater EROEI relative to amount of energy invested in the construction of the power plant which depends on how the produced energy is utilized. Figure 2 shows the percentage of energy converted by various system in relation to the energy invested in the plant.

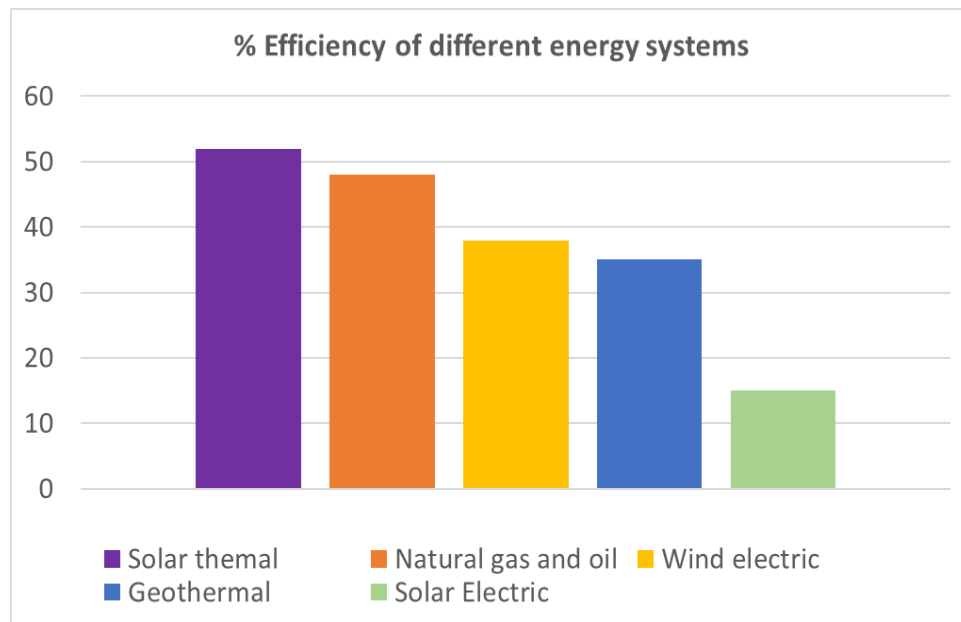


Figure 2: Bar chart showing energy efficiency percentage of different energy sources [8].

The graph shows thermal energy production from solar energy is most efficient whereas, solar electric energy is least efficient currently due to the storages devices required and inefficient use of produced energy. Although energy produced from natural gas and oil is moderately efficient but they use exhaustible sources which has urged scientists to find cleaner and efficient energy production sources.

From 2007 to 2035, the use of energy worldwide for electricity production, is expected to increase 3.0% each year and the share of renewable energy resources for generation of electricity is expected to grow from 18% in 2007 to 23% in year 2035 [9].

2.2.1 Detailed Analysis of widely used renewable energy resources

Fossil fuels are expected to become less readily available in the coming century. This will increase the cost of electricity produced by using them and further decrease their popularity and also the increasing concern regarding the adverse effects on the environment. Every energy production and transmission technology has an impact on the environment. However, conventional methodologies damage and pollute air, water, climate, land, landscape and wildlife and have considerably increased the level of harmful radiations. Recently, the drawbacks of CO₂ emission involved in the utilization of non-renewable energy resources to produce energy, and the climate change have accelerated the research and work regarding the use of renewable energy resources. The most significant renewable energy systems include solar energy (both thermal and electric), photovoltaics, biomass, wind, geothermal, ocean and hydroelectric systems [10].

a) Solar Energy

The amount of energy that strikes Earth within 1 hour is greater than the total energy consumed by humans during one complete year [11]. Solar energy has been proven beneficial for the environment compared to the conventional energy production technologies. One of the most efficient use of solar energy is the conversion of solar energy into thermal energy. Solar thermal energy is a term coined for the conversion of solar irradiance into heat. A typical solar thermal system uses solar concentrates and collectors to collect solar radiation, store it and later use it to heat air or water in industrial, commercial or domestic scale [12]. Figure 3 shows a schematic diagram of conversion of solar irradiation to mechanical energy.

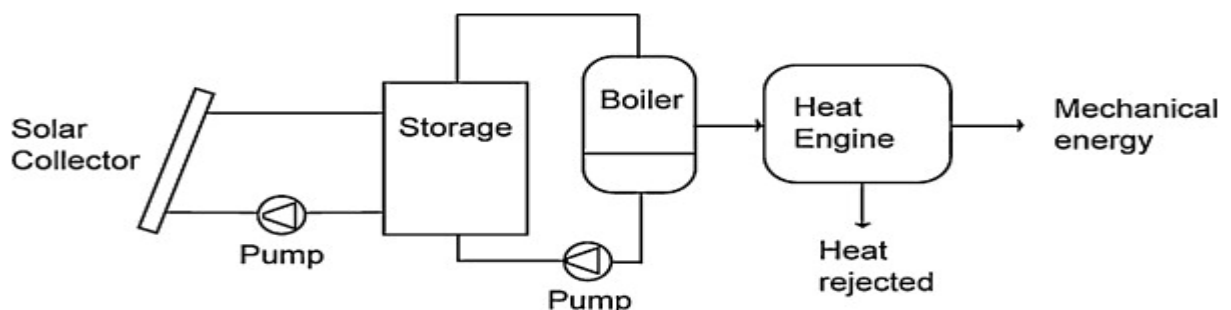


Figure 3: Schematic diagram of solar thermal conversion system [12].

The solar collector helps in collecting the solar irradiation and is fed to boiler to heat the medium that can be water or air and it is also stored inside storages to help in days with minimum solar irradiation. In order to increase the overall efficiency of solar-thermal systems, solar collectors heat air or water act as the medium for transferring heat. The heat generated is used to run the engine which produces mechanical energy for various industries such as dairy, textile, tanned food and chemical etc.

One of the significant advantage of solar energy technologies is the reduction in CO₂ emission. Furthermore, no contaminating waste product is released into the environment during the operation. Solar energy has also enabled the reclamation of degraded land. Less transmission lines are required for electricity grid because it is local [13].

b) Photovoltaic System

PV (photovoltaics) effect was discovered by Becquerel in 1839 while studying and analyzing the impact of light on electrolytic cells [14]. Solar energy is harnessed by converting the energy of sun into electrical energy and photovoltaics are capable of converting solar energy directly into electricity [15]. Establishing a photovoltaic system depends on various key factors such as solar irradiation, load requirements and geographical location. Schematic diagram in Figure 4 shows the general setup of a stand-alone photovoltaic system.

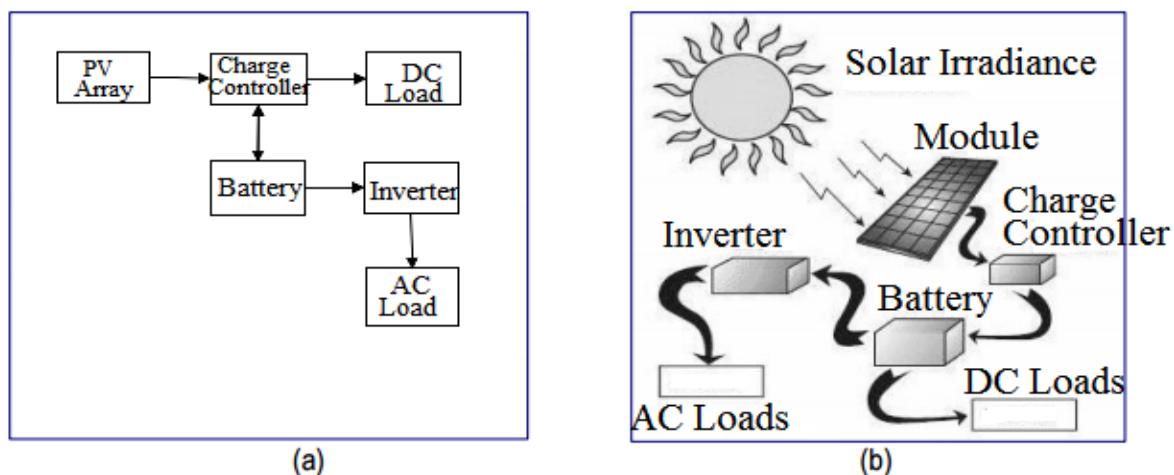


Figure 4 a) Block Diagram b) Schematic Diagram of a stand-alone photovoltaic System [15].

The system shown in Figure 4 above, operates independently without any interference of the electric grid and it can supply a certain amount of AC and/or DC output. A reservoir of batteries is utilized to store electrical energy to be used later at night or during days with no sun. However, systems that are connected to the electrical grid sometimes referred as utility-interactive systems, they get their power from the grid to enhance the power output of the system when needed and in reverse case if the output power of the photovoltaics is a surplus, then the additional output is sold to the utility [15].

Photovoltaic systems are gaining popularity in both developing and developed countries. The modules of photovoltaic systems are solid-state devices that are capable of converting sunlight directly into the form of electricity. No rotating equipment is required. The main advantage of photovoltaic systems is that they can be built in any size, they need minimal maintenance and are reliable [16].

c) Biomass Energy

Sunlight, water, and CO_2 present in air react during the process of photosynthesis to form carbohydrates that make up biomass in plants. Efficient processing of biomass can be done either biologically or chemically. The energy that is stored in the chemical bonds can be extracted when it combines with oxygen to form CO_2 . These reactants are not contaminating atmosphere and moreover, they prove to be beneficial as the CO_2 produced is used to produce more biomass and water adds on to the moisture content of the atmosphere [17]. Furthermore, when biomass is produced by means of sustainable methods, the amount of carbon dioxide emitted during conversion process is approximately equal to the amount of carbon dioxide take which is summarized Figure 5.

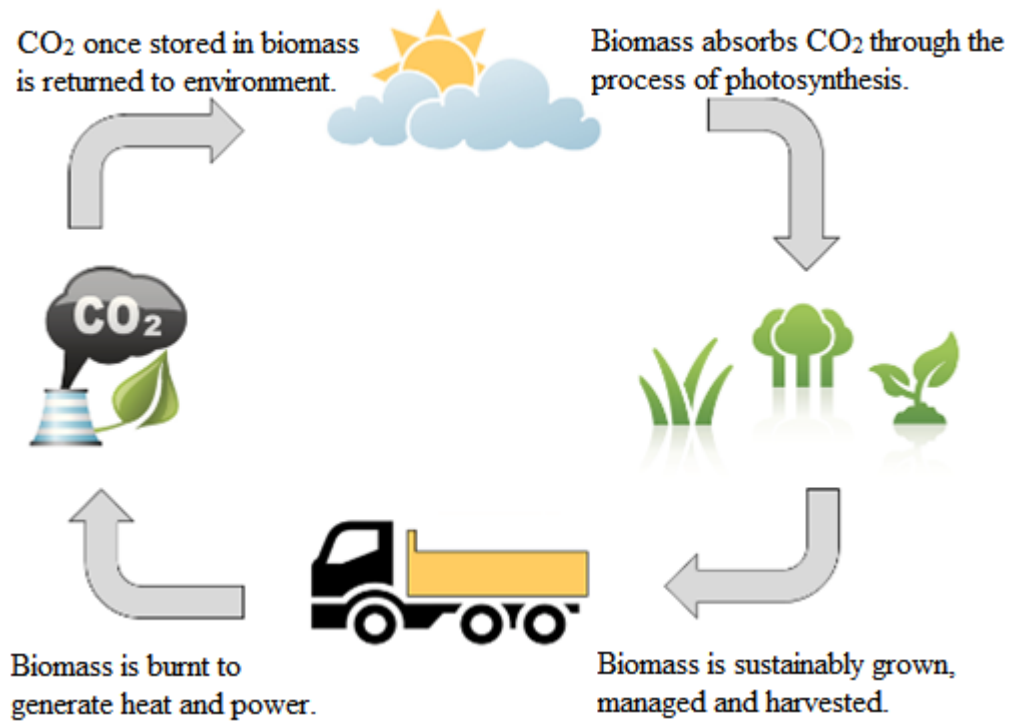


Figure 5: No net increase in atmospheric CO₂ level during biomass production cycle [18].

Biomass is a natural carbon neutral process which means that biomass works as a carbon sink by constantly adding and removing carbon from the atmosphere. During decaying and burning, the carbon dioxide stored in the biomass through photosynthesis, is released. On the contrary, burning of fossil fuels release ancient geological CO₂ stores and other greenhouse gases which result in an imbalance in the natural carbon cycle of the Earth. Biomass can be derived from various sources such as herbaceous plants (grasses), woody plants, manures and aquatic plants. Biomass holds a potential of producing 30 EJ/yr using agricultural and forest residues worldwide whereas, the annual amount of energy demand is 400 EJ [17].

d) Energy derived from Wind

Wind energy is a clean, abundant, environmentally friendly and affordable renewable energy resource [19]. Wind energy can be used in both large-scale wind turbines to enable utility applications and small-scale wind turbines that can be used for on-site energy generation [20].

Wind energy is a strong competitor against coal or nuclear power systems considering the amount of pollutants and contaminants produced by the latter [21]. Furthermore, the cost of wind energy is decreasing considerably compared to other energy producing technologies. There are no fuel costs for wind turbines as wind is a natural fuel. Figure 6 shows the main components of a wind turbine.

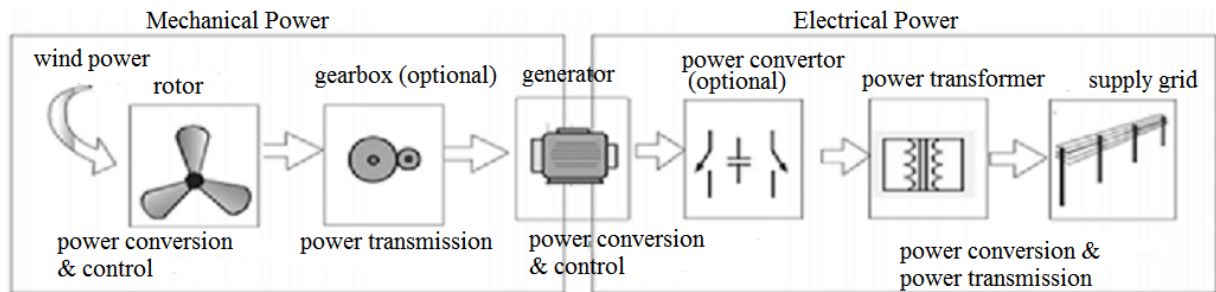


Figure 6: Main components present in a wind turbine [22].

Generally, wind turbines are composed up of a turbine rotor, generator, gear box, a power electronic system and a transformer grid to establish connection. Wind turbines harness wind power by utilizing turbine blades and convert the wind power to mechanical power. Mechanical power is converted into electrical power by the generator. This electrical power is fed into a grid by power electronic convertors and a transformer which have a circuit breaking system and electricity meters [22]. The efficiency of wind turbines depends on three factors that are its rotor diameter, its type which means whether it has a horizontal axis or vertical axis and wind speed [8].

e) Geothermal Energy

Geothermal energy is referred to the energy that is contained in the Earth's core. The heat travels from the interior of Earth to the surface. Magma is present in the core, which is constantly cooling down and releasing heat. However, in those areas where magma is not present, heat accumulation takes place due to geological features of the crust, which enable the geothermal gradient to increase. Apart from being cleaner, geothermal electricity is also cost-effective [23]. Three types of geothermal power plants are currently in use namely, dry steam power plant, flash steam power plant and binary cycle power plant and their differences are outlined in Figure 7.

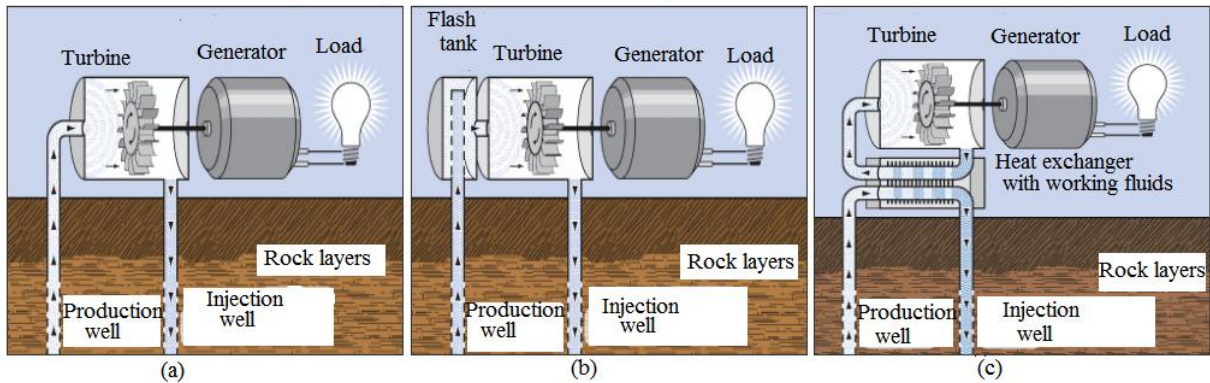


Figure 7: Three types of geothermal power plants: a) Dry steam power plant, b) Flash steam power plant, c) Binary cycle power plant [24].

Dry steam plants collect steam directly from a geothermal reservoir which then drives the generator turbines. Flash steam plants, on the other hand, are run by hot water collected from deep inside the earth. This hot water is converted into steam to drive the generators. Later the steam condenses to water when it cools down and this water is injected back into the ground for reuse. However, in binary cycle power plants, the heat from geothermal hot water is transferred to another liquid. The second liquid vaporizes due to the heat and in turn derives the turbines [24].

f) Hydropower energy

The development of hydroelectricity dates back to 20th century and it was usually related to the construction of large dams. Massive barriers were built using concrete, earth and rock placed across rivers in order to create artificial lakes of huge capacity [25]. Hydropower energy is among the most maturely stable and advanced form of technology. It provides electricity in one form or another in over 160 countries [9]. Hydropower plants transform the potential energy stored in water due to height, into electricity. Total technically harnessed hydropower potential is estimated to be about 16500 TWh per year [9]. Compared to all the available renewable energy resources, hydropower energy production is cleaner and more efficient and it accounts for 19% of all the electricity produced worldwide [25].

2.2.2 Drawbacks of current electricity producing technologies

Although energy producing procedures using renewable energy sources have less polluting effects, they are not free from drawbacks which are discussed below for popular renewable energy resources.

a) Solar Energy

Solar energy has few drawbacks, which include the visual effect on the aesthetics of buildings. It may also release accidental chemicals during operation such as silane and trimethylgallium. This may lead to water pollution if these chemicals seep into water bodies. Often, there is a need for large areas in order to establish a solar power system. This reduces the space for cultivable land. As solar energy is not available for 24 hours a day, additional measures are taken for some applications which can accumulate solar irradiation inside an embedded phase transition during sunny days. This is later released in a controlled system in case of severe conditions [12]. Furthermore, during the construction of solar modules, toxic and flammable materials may be utilized. There are slight health risks associated with solar energy systems not only during manufacturing, but also safe disposal of waste products and remains [13].

b) Photovoltaic System

Photovoltaic systems are becoming widespread, but they are not free from drawbacks and challenges. Shockley and Queisser analyzed the limiting efficiency of solar cell in 1961 and according to them the thermodynamic efficiency of a single homojunction cell was approximately 31% [14]. This limitation is caused by the transmission losses of photons having energies below bandgap and photons having higher energy compared to the bandgap cause thermal relaxation of carriers which is also a factor for loss. The cost of a PV module depends on two main factors that are conversion efficiency and total cost of manufacturing of the module per square area [14]. The current efficiency achieved by various PV technologies is tabulated in Table 2.

Table 2: Efficiencies achieved through different PV methods [14].

PV technology	Efficiency (%)
---------------	----------------

CIGS (Copper indium gallium selenide) thin film	19-20
CdTe thin-film solar cell	16-17
Si polycrystalline thin-film solar cell	16-17
III-V multi-junction solar cell	40

As shown in the table, the efficiencies achieved are not high enough to meet the energy demands and the rest of the energy is lost in undesirable forms of energy. Furthermore, the optimal size of solar panels needs precise calculations and it is the most critical factor. Care has to be taken when choosing the backup battery as the capacity of the battery should be able to withstand the load demand. Furthermore, solar insulation should be available at the desired location as the percentage of power generated is dependent upon the solar isolation [26]. The overall efficiency of a PV system is strongly affected by the variations in climatic conditions such as availability of solar irradiance and ambient temperature [26]. Large PV systems can have an adverse effect on the ecosystem. Moreover, installation and parts of any photovoltaic system are costly [16].

c) Biomass

There is a time lag between the instantaneous emission of CO₂ due to burning of fossil fuels and its uptake in the form of biomass. This time lag can take several years and the fact that biomass is not replaced by replanting at the pace it is being used which is only increasing this time lag even more [17].

d) Energy derived from Wind

Wind energy systems depend on wind speed and accurate wind data is required for higher efficiency but it is at stake because of lack of investment in collecting precise wind data. Moreover, public acceptance also faces challenge since wind energy based products have a strong environmental impact and can cause visual and noise distraction [27]. Although turbines with larger diameter rotors produce significantly more power with an increase in wind speed, they are subjected to higher amount of mechanical stress. This makes large diameter rotors risky during higher wind speed. Wind turbines are not capable of taking full advantage of the total wind power and according to Betz' law wind turbines can only benefit up to 60% of the wind

power however, in practice the efficiency of wind turbines drops to 40% for higher wind speeds. The remaining energy density of wind is not harnessed and lost as a result. Figure 8 shows major energy losses in different parts of a wind turbine.

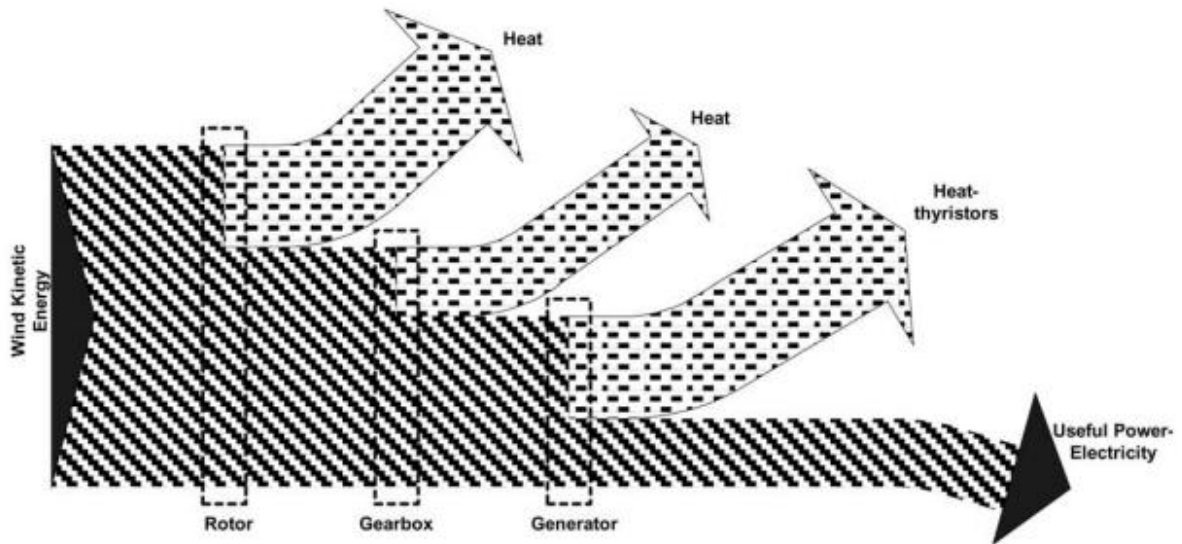


Figure 8: Loss of energy in various components of a wind turbine [8].

As seen in figure above, the energy is mainly lost in the form of heat which causes additional friction between the bearings and the shaft. In addition, it also results in the heat that is abducted from the gearbox by the cooling fluids, the cooling fluid in the generator abduct from the gearbox and the thyristors which helps in starting the turbine smoothly however, 1-2% of the energy that passes through these components is lost [8].

e) Geothermal energy

Although geothermal energy is categorized as a renewable energy resource but if time scale used in normal human society is used, geothermal energy resource cannot be termed as entirely renewable. This is because the shut-in pressure that is measured at a geothermal site keeps on declining due to extraction of fluid and the depletion of the reservoir. Geothermal energy can only be successfully termed as renewable energy if the rate at which the heat is extracted does not exceed the replenishment rate of the reservoir i.e. at the rate the reservoir is refilled [23]. Safe disposal of the cooled fluid is yet another drawback of geothermal energy. During

electricity production using geothermal energy, steam that condensates into water contains a high percentage of salts and needs proper treatment prior to disposal [23].

f) Hydropower

Hydroelectric power plants have proven to be unsustainable when it comes to their effect on environment. The prime concerns include the change of the hydrological regime, which puts at stake the activities occurring downstream of the water reservoir. Furthermore, the water quality is sacrificed due to difficulty of decomposition of toxic wastes. Large-scale deforestation in order to establish a water reservoir cannot be overlooked. Hydropower systems actively contribute to the emission of greenhouse gases because of the decomposition of plants that are completely submerged in water [28]. Heavy rainfall can increase the level of water in the reservoir and may lead to severe flood. Moreover, the water reservoir can become a breeding ground for vectors such as mosquitoes, that carry endemic diseases due to the formation of backwater [28]. There is another risk factor involved that water may be used mostly for electricity production and is not rightfully used for multiple purpose such as fish breeding, farming and irrigation.

2.3 New alternative for electricity production

The high demand of green energy has spurred the need to research about new innovative renewable energy resources in order to produce electricity such as lightning, water present in air in the form of rain and moisture, graphene sheets on rooftops and Hygroelectricity.

a) Lightning

Harnessing electricity from lightning is relatively new research field. However, it is highly controversial due to the safety concerns regarding lightning strikes. Some of the primary objections include the facts that lightning is not available on demand, the frequency of lightning changes from region to region, it is difficult to direct lightning strike, lightning is unpredictable and dangerous and may destroy the equipment in use. Lightning occurs really fast and makes charge built up difficult [29].

Despite the concerns, there has been a substantial amount of research in this field. Researchers have come up with various ideas to capture lightning to produce electricity and the most popular ones are building a tower that will be tall enough in order to attract lightning. The tower has to be considerably conductive enough to guide the captured lightning strikes. However, it is still not confirmed whether the material present at the point of lightning strike will vaporize or if it should be a particular size and shaped in such a way that it is able to transmit the lightning strike without getting destroyed itself during the process [30].

A second approach which is successful and well-studied is to direct a rocket into a storm and target a lightning strike. A cable is attached to direct the strike, which vaporizes on contact with lightning [31].

Third technique proposed is to use laser for lightning targeting. Ultrashort pulse lasers have high peak intensity which enables them to generate continuous long plasma channels with a considerable amount of energy. These channels may be used to trigger and guide a positive leader from ground rod, facing upwards. This positive leader would later form a connection with a negative leader descending from a cloud. Hence, catch bolt of lightning when it is formed [32].

Fourth technique relates to quantify the electricity in a lightning strike and it is critically important to take into consideration the high amount of energy and a short pulse of time in the order of microseconds [33].

b) Rain

Energy harnessed from raindrops is among renewable energy sources in tropical countries like India, Malaysia, Brazil, where the yearly amount of rainfall is recorded to exceed 2000 mm per year [34]. Raindrop carries energy mostly in the form of kinetic energy, which is converted into mechanical vibrations when the raindrop hits a hard surface. These mechanical vibrations can be captured by piezoelectric materials, which have an ability to convert the mechanical energy into electrical energy due to their unique property known as direct piezoelectric effect [35]. When a piezoelectric material experiences tensile stress, an electric field is generated due to the asymmetric structure of each unit cell of a piezoelectric material. The generated electric field

results in flow of current across the material and this makes piezoelectric materials suitable candidates for harvesting kinetic energy in raindrops [36].

Energy harvested using piezoelectric materials is categorized as micro energy and is only in the range of mW or μ W. Hence, piezoelectric harvesters are beneficial for small-scale energy generation, which can be used to provide power to self-powered sensors and small scale electronics [37] that require a low load. Research is still ongoing to find combination of most efficient piezoelectric harvesters. Currently, the efficiency of mechanical to electrical energy conversion achieved by piezoelectric harvesters is less than 1%. However the simulation carried out by Guigon [38], promises conversion efficiency up to 2.5% and recent studies regarding harvesting piezoelectric energy using constant vibration sources [39] have shown that theoretically it is possible to attain 46% energy conversion. Piezoelectric conversion efficiency can be further optimized by searching for best piezoelectric materials combination, shape and size of transducers and the interface circuit to achieve maximum energy output with less loss such as loss of raindrop due to splashes.

c) Nano-modules in Solar Energy Harnessing devices

Nano-engineered materials are made up of structures that have dimensions in nanoscale. One such material is polycrystalline structure that is composed of nanosized crystallites. Nanostructured materials play a vital role in harnessing solar energy by solar cells due to their specific chemical and physical properties. Generally, the addition of nanostructured materials has proved to be beneficial in photovoltaics by improving the efficiency of solar cell in two ways [40]: firstly, it is able to control the energy bandgap which in return makes it more flexible and inter-changeable, secondly, nanomaterials increase the active optical path and decreases the chances of charge recombination significantly.

Physical properties related to size of nanostructured materials include large surface to volume ratio which makes nanomaterial more reactive and results in a strong influence on the properties of the structure. They have shown a theoretical improvement of 60% in the efficiency of solar cells [41].

Semiconductor nanostructures are also known as quantum dots, which include PbS, PbTe, PbSe, CdSe, CdS, Si etc. Under normal conditions, semiconductor materials are only able to generate one exciton after it absorbs a photon and the photon with high excitation energy is wasted due to emission of photon [40], however, MEG (multiple excitation generation) effect has enabled the generation of many excitons. This may help in improving the efficiency of energy conversion achieved by solar cells composed up of nanocrystals [42].

Other nanomaterial systems are also available for harnessing solar energy such as DSSC (Dye-sensitized nanostructured solar cells) shown in Figure 9. They mimic the process of photosynthesis which is based on the chlorophyll dye. It can produce more than 7% efficiency by successfully combining nanostructured electrodes and charge injection dyes [43]. The solar cell named Grätzel cell. Dye-sensitized cell shown in Figure 9 works on photoelectrochemical principles. Liquid phase electrolyte or some ion-conductor is used as a transport medium for charge.

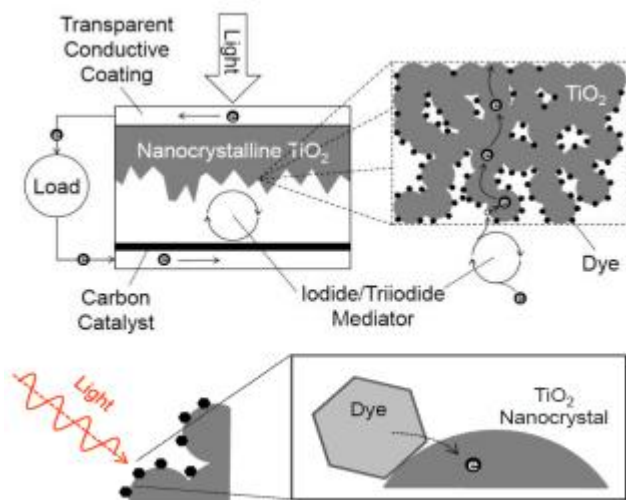


Figure 9: Configuration of Dye sensitized cell and its electron transfer mechanism [40].

The incident photon is absorbed by the molecule of dye present on the surface of nanocrystalline particles of TiO₂ and excites an electron of the dye from the ground state to the excited state. The excited electron is inserted inside the conduction band of TiO₂ particles and the dye molecule is left with an oxidized state. This electron that is injected, penetrates through the

transparent conductive coating of the glass and then passes through an external load to the positive electrode where it is transferred to the triiodide mediator to produce iodide. The cell is regenerative as the oxidized dye is reduced by the iodide in the electrolyte [43].

Quantum Dots solar cells are also used to harness solar energy. They are nanocrystals having zero dimensions and are usually constructed by using direct bandgap semiconductors [40]. They have unique photophysical and photochemical properties that are beneficial for the development of chemical and biosensors. Quantum Dots have improved resistance against multicolor fluorescence and photo bleaching. Tetrapod design of quantum dots (Figure 10) having four arms and a core, demonstrate better charge transport. It can be tuned both lengthwise and widthwise.

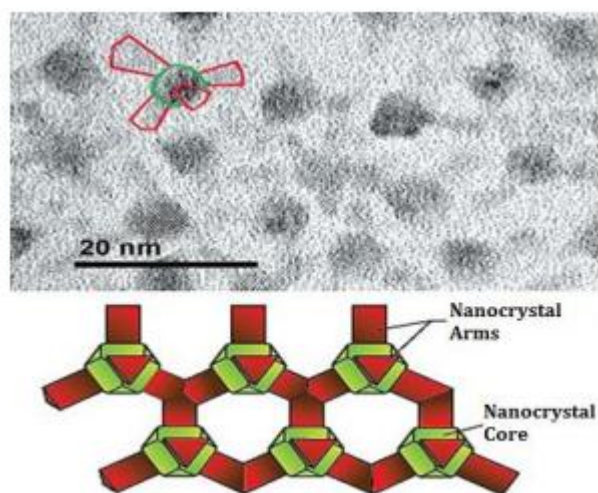


Figure 10: Diagrammatic representation of Quantum Dots (tetrapods) [40].

The overall cost of Quantum Dots can be significantly reduced in the future as they can be manufactured using inexpensive and simple chemical reactions. They could be used to manufacture thin-film photovoltaics that could possibly be more efficient compared to the conventional silicon cells as nanocrystals that are composed up of certain. Moreover, if their size and shape is changed they can absorb different color of light. It is possible to tune the band gap of quantum dots which enables the creation of intermediate band gaps. Theoretically it is possible to achieve a maximum efficiency of 63.2% with this method [40]. When a photon of light travels through the solar cell, it strikes a particle of quantum dot and raise the energy if few

electrons present in the quantum dot. After they are excited, the electrons penetrate inside the titanium dioxide and pass through it and finally reach the electrode's conducting surface as illustrated in Figure 11.

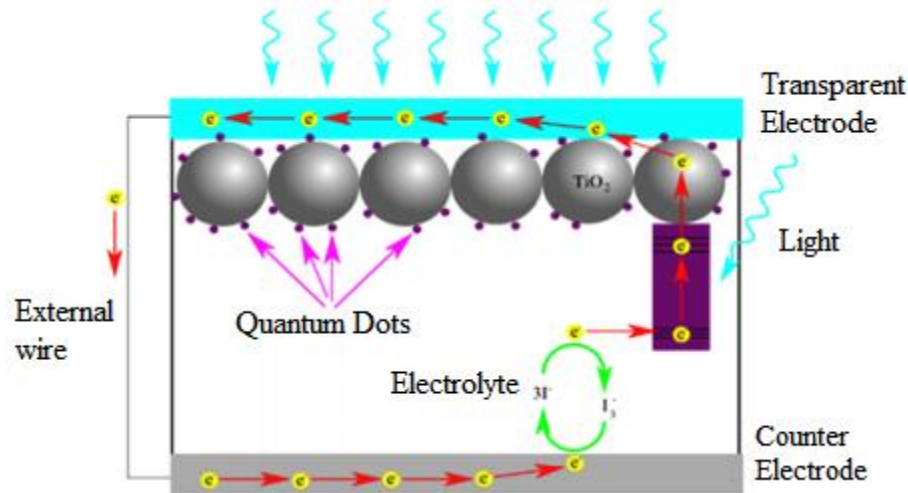


Figure 11: Configuration of Quantum Dots solar cell [40].

As the electrons are traveling towards the electrode's conducting surface, they leave behind holes in the quantum dots ready to be replaced by other electrons. In order to fill these holes, the quantum dot collects electrons from the electrolyte. This causes a depletion of electrons in the electrolyte which in return collects electrons from the other electrode. Thus whole process causes a voltage to develop across the solar cell and induces current [40].

Another type of solar cells based on nanotechnology is Carbon Nano Tubes (CNTs) solar cell. Carbon nanotubes are tubes having dimensions corresponding to molecular scale. They consist of carbon atoms arranged in hexagonal lattice structure and have exceptional electrical and mechanical properties. The structural configuration of nanotubes can be defined with the help of vectors notation with n representing rows and m representing columns which shows how the sheet of graphene is rolled as shown in Figure 12.

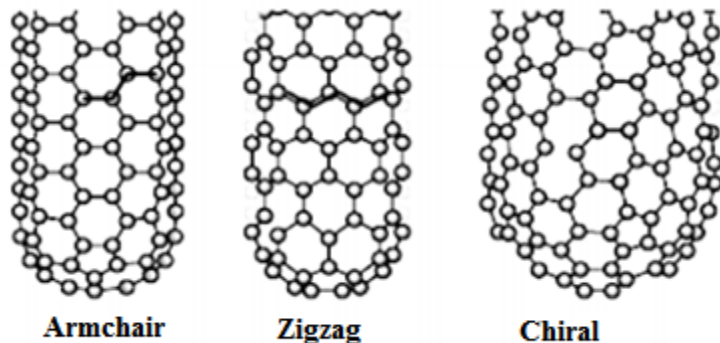


Figure 12: Diagrammatic structural configuration of carbon nanotubes [40].

In photovoltaic cells, nanoscale tubes can be used to generate an electric current if they are coated with specific n-type and p-type semiconductor junction materials. This would in return increase the overall surface area available to generate electricity [44].

d) Hygroelectricity

Hygroelectricity is an innovative energy production topic where certain materials are designed to capture electric charges which builds up on isolated metals when placed in atmosphere, which is a potential reservoir of OH^- and H^+ due to the presence of humidity and dissociation of water. When these charges transfer to the isolated metals, they result in a net charge. The charge is directly proportional to the percentage of relative humidity in the atmosphere [45]. This phenomenon led to the possibility of capturing electricity from air which was a dream of famous scientist Nickolas Tesla. In the recent years, various publications have enabled to prove that ions [46, 47] and electrons [48, 49] participate in electrostatic charging under numerous conditions.

In numerous systems, the relative humidity percentage has shown to be directly related to the amount of buildup and dissipation of charge. Hence, the charging is faster in environments with higher level of RH compared to dry conditions [45]. When isolated metal samples are exposed to water vapor, it leads to the buildup of charge on the metal. This effect was observed first in the Institute of Chemistry of University of Campinas, Brazil by Fernando Galembeck and his team [45] during Faraday cup measurements to control the charge present on insulators, which

were studied using Kelvin Probe Scanning Microscopy. The results showed a significant effect of relative humidity on patterns of charge distribution on metals and dielectrics [50].

Theoretically, electric charge present on an isolated metal sample should continue to be equal to zero after the metal sample is grounded. However, if the isolated metal sample is exposed only to external fields created due to high-energy ionization radiation, charge will build up in it just like in Faraday cups used to detect electrons and radiations [51, 52].

According to the research carried out by Fernando [45], if the metal sample under observation, is made out of brass (Cu: 64.1 % and Zn: 35.9%), or electrolytic copper fixed inside a hollow chrome-plated brass (CPB), but isolated and grounded from the top cover, the charge moves slowly to the negative values irrespective of the amount of RH. This means that any change in the RH values will not have a significant effect on the rate at which charge changes. However, a different behavior is experienced when the sample under observation is composed up of aluminium, stainless steel (SS) or SS screen. When the sample is exposed to low humidity values, there is a slow drift in charges as in copper and brass case. However, the main difference is observed at higher values of RH, when the charge drifts quickly. Aluminium and CPB display similar behavior and achieve a negative charge when the value of RH increases but SS attains a positive charge as the relative humidity value is increased [45]. From this information, it can be deduced that there is a connection between the rate of water absorption and charging of metal. This was further verified by Fernando by applying a coating of silicone oil on outer surfaces of aluminium and SS cylinders. The oil coating caused a delay in the contact between the water vapour and the metal surfaces. The buildup of charges on the coated metal samples could be neglected up to the level when RH reached 95%.

The above-mentioned observations led to the possibility of generating electricity by inducing charges in metal samples placed under high humidity. This was verified by Fernando by constructing a device composed up of precise order of sheets of filter paper stacked on top of each other, aluminium, filter paper, stainless steel and lastly filter papers. These stacks account for capacitors with electrodes made up of two metals coated with layers of oxides, which show different adsorptive behaviors. The electrodes are separated by a dielectric of porous nature which has a high capacity of absorbing water vapour. They were then mounted inside a grounded

aluminium box kept inside a Faraday cage. Both electrodes were connected to an electrometer. When the humidity was increased, a steep increase in voltage between both metal sheets was observed as shown in Figure 13.

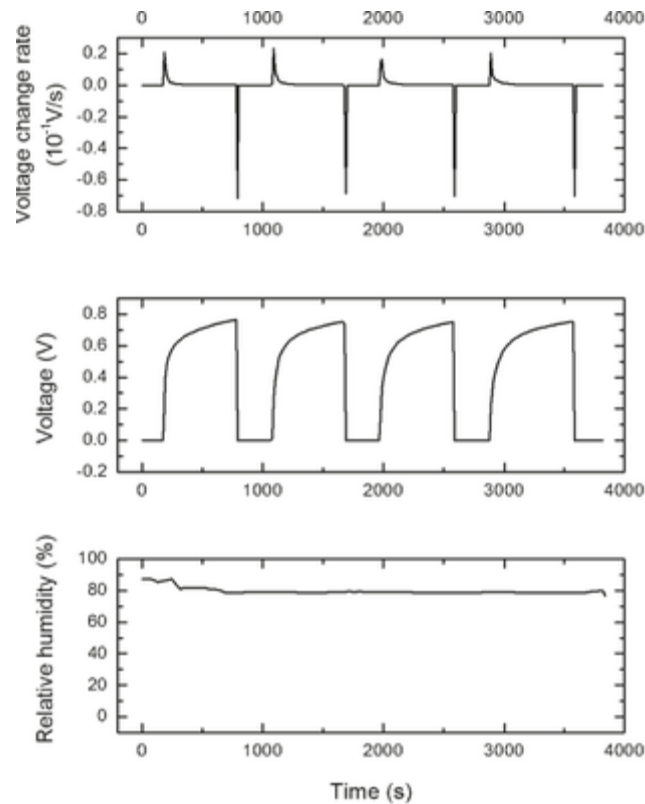


Figure 13: Charge-discharge cycle of capacitors composed of two metal sheets (SS and aluminium) with a cellulose sheet separator and enclosed inside two cellulose sheets under humid N₂ atmosphere [45].

Aluminium, SS and chromium attain charge when placed under high humidity and are famous for their good resistivity to oxidation. This is because of the protection provided by coating metal from the atmospheric effects. Water vapor is absorbed in the oxide layer that leads to significant changes in the structure [53].

Cr and Al oxides are amphoteric in nature which means they can react with both acids and bases. Layer of aluminium oxide on metals have O and OH sites that follow the Bronsted/Lewis acid-base properties, which are considerably independent of the oxidation process [54]. However, dry aluminium generally demonstrates marked acidic characteristics [55]. Hydroxyl groups are present in mixed aluminium-chromium oxides that are prepared using sol-gel methodology to be used as catalysts to depict a contradictory acid-base behavior. Chromium oxide sites have basic nature and aluminium oxide sites have an acidic nature [56]. Hence, when both of these two oxides are formed, the H^+ ion favors to binds to Cr oxide. However, Al^{+3} ion also collects OH^- ions from aqueous solution. Water itself is amphoteric in nature, and acts as acid or base under different conditions. Water molecules that are absorbed contribute in providing either H^+ or OH^- ions to the surface of metal samples coated with a layer of oxide, which depends on its state and nature. Thus, it imparts an overall charge on the surface of the metal sample. This explains that the charging of metal under high level of humidity is due to few acid-base reactions that occur on the surface such as:



Where S signifies surface sites and the OH^- or H^+ ions are released into the surrounding atmosphere which are bound to the clusters of desorbed water molecules. OH^- or H^+ ions that are derived from absorbed water could be present beforehand in gaseous phase in the form of ionic water clusters [57]. A significant concentration of ions in the gas phase increase their absorption which leads to contribution of charge present on the metal sample. The adsorption and desorption of the water molecules to and from the metal sample, which depends on the acid-basic nature of the oxide layer on it, imparts a positive or negative charge onto the metal [45]. Results achieved by Ducatui et al. [45] have proved to be a vital pillar to demonstrate the role played by water as a reservoir of charge for solid, which initially was considered solely for dielectrics, but now has been further extended to include metals also. Figure 14 shows a schematic representation of the exchange of charges.

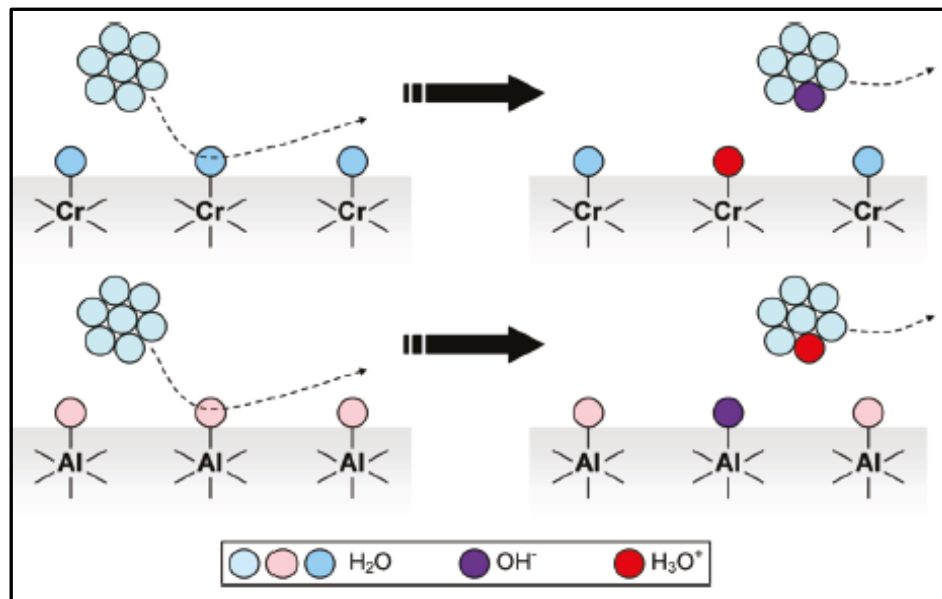


Figure 14: Charge transfer mechanism from the atmosphere to surface of metal [45].

On the top, formation of a positive charge is depicted over a basic oxide and in the bottom of the figure, negative charge formation is occurring over an acidic oxide layer. Water molecules are neutral and amphoteric in nature so they tend to combine differently with oxides depending on their acidic-basic characteristics. This is a matter of high significance to understand how the growth of water layers that is absorbed on most surfaces result in changing the overall electrical nature [58].

Another successful experiment conducted by Gouveia and Galembeck in 2009 [59], proved that electric potential varies with a change in relative humidity within a closed system that is electrically isolated and grounded. Films of noncrystalline silica and aluminium phosphate were investigated using Kelvin probe force microscopy (KPFM). Relative humidity was increased from 30% to 50% and then 70% which was then decreased back to 30%. The comparison of KPFM electric potential of sample at each relative humidity value showed that the amount of average electrical potential increased with an increase in the value of relative humidity and it decreases when relative humidity value is decreased as shown in Figure 15 where x-axis shows the line-scan distance (nm) and y-axis represents electric potential (V). Distance (a standard

feature of all SPM scans) means the location (coordinates) on the sample where electric potential was measured.

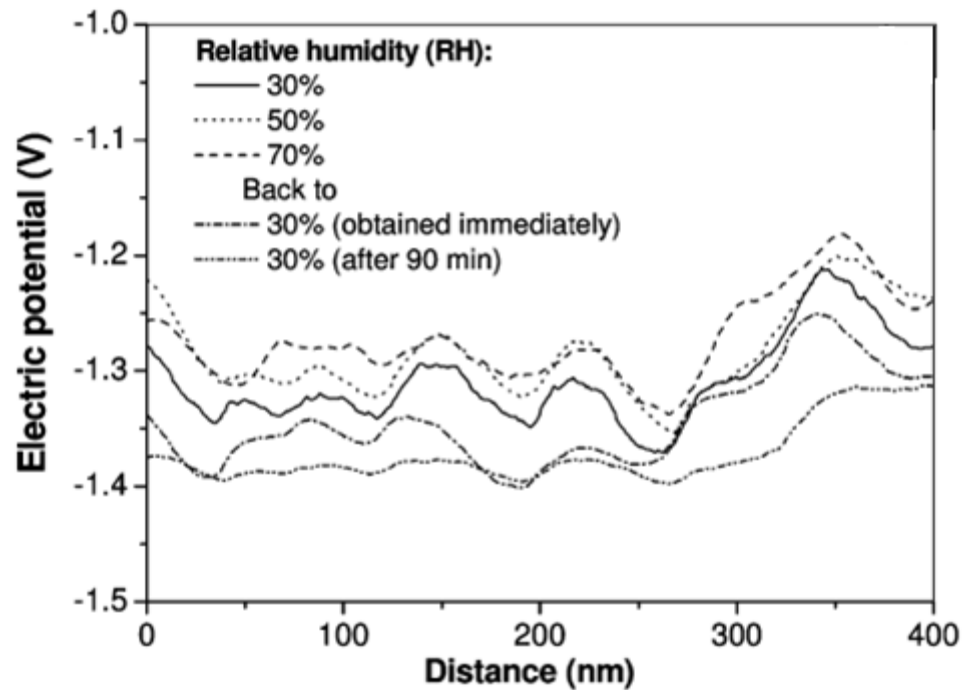


Figure 15: Variation of electric potential of aluminium phosphate particles at different relative humidity value [59].

According to the Figure 15, the electric potential was maximum at 70% RH and minimum for 30%. The electric potential became more negative when the humidity was decreased from 70% to 30% which is because the amount of water desorption increases the overall charge in the sample even when the system is grounded.

A similar experiment was performed using Stöber silica particles and variation in the value of electric potential was observed while changing the amount of relative humidity as shown in Figure 16. However, silica particles showed an overall shift towards negative electrical potential under higher humidity conditions.

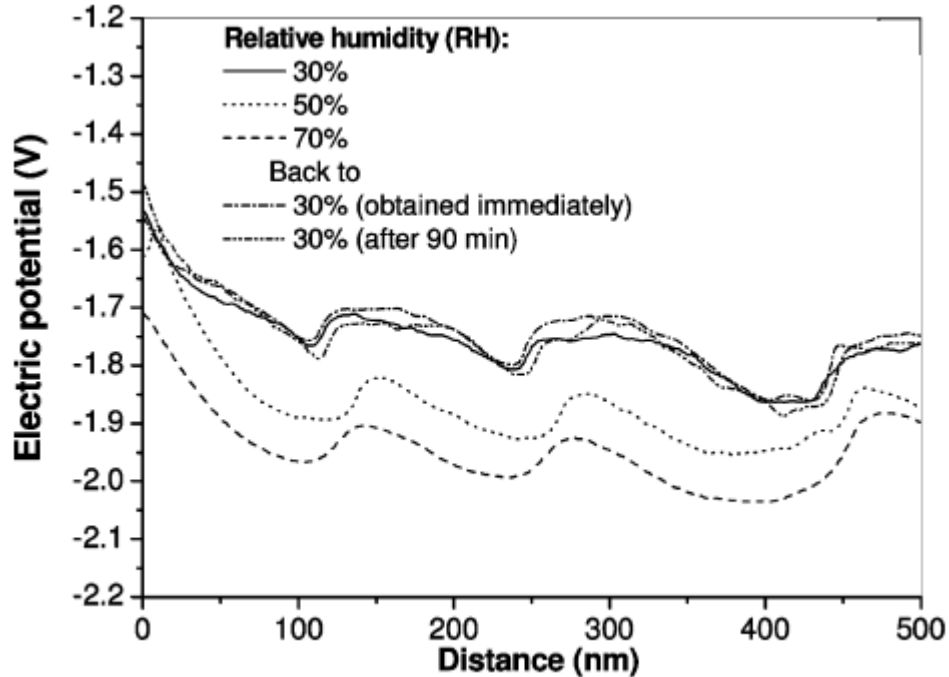


Figure 16: Variation of electric potential of Stöber silica particles at different relative humidity value [59].

As shown in Figure 17, value of electric potential was more negative for 70% RH and less negative when RH was decreased to 30 %. The difference in electric potential was less when value of humidity was increased from 30 % to 70 % but large reverse was observed when the value of humidity was returned to 30 %. This shows that Stöber silica particles have more repeatability compared to aluminium phosphate particles.

Both experiments show repeatability and variation of electric potential with a change in relative humidity. This can be explained by assuming that ion partition is related to the adsorption-desorption phenomenon. Clusters and desorbed water molecules carry an excess positive charge despite overall negative potential of the sample. The results of this experiment verify that the atmosphere acts as electrostatic charges' source and sink in dielectrics due to splitting of OH^- and H^+ ions. This is because of water adsorption and hence atmospheric humidity is a source of charge which can be harnessed [59].

Recently, more research has been conducted to study the relationship between humidity and electrical potential. In May 2017, ZrO_2 nanopowder doped with 3 mol % Y_2O_3 were studied by

Doroshkevich et al. [60] to investigate the effect on electrical potential during humidification. They studied the relationship between variation of weight of the sample by absorbing water and the electrical potential generated as shown in Figure 17.

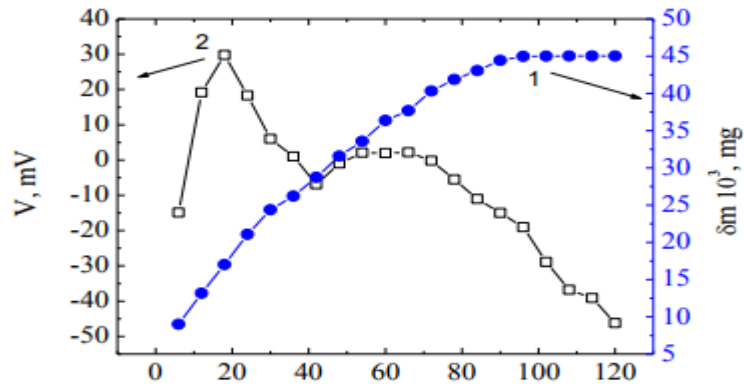


Figure 17: Variation of (1) weight, δm (mg) and (2) electric potential, V (mV) with time (min) [60].

As seen from Figure 17, when weight changes due to humidification, the value of electrical potential also varies which supports the concept of Hygroelectricity. Similar results were achieved by Bikov, 2016 [61], during his Master's thesis when he investigated zirconia nanocomposites. Electric potential of samples containing different amount of ZrO_2 were studied while changing the value of humidity around it from 3 % to 18 % and the result are shown in Figure 18.

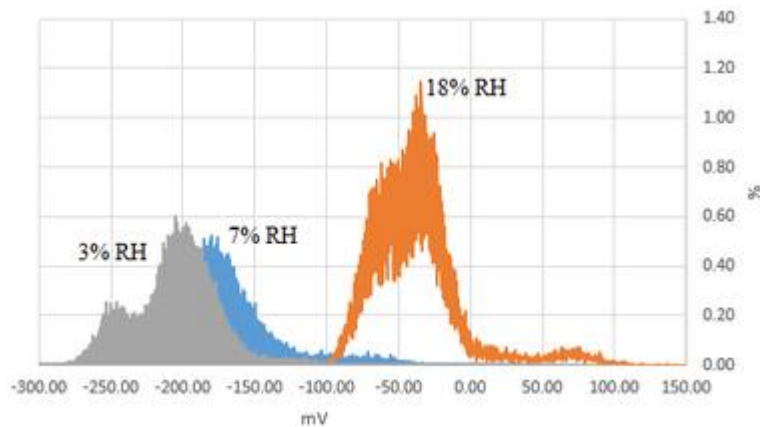


Figure 18: Variation of electrical potential when changing relative humidity from 3 % to 18 % [61].

As seen from Figure 18, value of electrical potential varied as humidity was changed. These results open a whole new approach to harness electricity from atmosphere. Metals and alloys can be used conveniently to trap charge present in atmosphere and transfer them to circuits and specially designed devices. It may also help to design new and better protective and precautionary measures for electrical circuits of vast range of sizes. These researches carried out by Galembeck and other researchers laid the foundation for this Master's thesis to test if similar results can be obtained by zirconia when RH is changed for a larger range i.e. 0 % to 100% in a controlled environment.

2.4 Electric potential at nanoscale

At the moment, various nanomaterials are under critical research, in order to fully exploit the benefits available at the nanoscale. However, few of them have been discussed below due to a time constraint.

The discovery of freestanding form of nanoscale graphene was made in 2004. However, despite its comparatively young age, graphene has secured its attractive position in scientific community due to its unique electrochemical, optical, electronic, thermal and mechanical properties and diverse applicability in various industrial processes. One of the most important characteristics of an electrode material is the surface area it has. Surface area is significant parameter for various applications such as bio-catalytic devices, energy storage devices and sensors. It has been theoretically proved that graphene has a surface area of $2630 \text{ m}^2\text{g}^{-1}$, whereas surface area of graphite is $\sim 10 \text{ m}^2\text{g}^{-1}$ and carbon nanotubes have a surface area of $1315 \text{ m}^2\text{g}^{-1}$ which is half the surface area of graphene [62]. Moreover, the calculated value of electrical conductivity of graphene is $\sim 64 \text{ mS cm}^{-1}$, which is 60 times greater than the electrical conductivity of single walled carbon nanotubes. Additionally, the electrical conductivity of graphene continues to be stable over a huge range of temperatures ranging as low as temperature of liquid helium [63]. Graphene has a distinctive bandgap, which renders the quasiparticles present in it and makes it identical to Dirac Fermions that are considered to be massless [62]. Another interesting electronic property of graphene is its ability to display half-integer quantum Hall effect with its Fermi velocity $v_F \approx 10^6 \text{ m s}^{-1}$ (effective speed of light) and this can even be observed in graphene

placed at room temperature [64]. In addition, it is possible to control the charge density of graphene by dint of a gate electrode [65]. For instance, the mobility of ultra-high electron has been attained in suspended graphene [66] and motilities exceeding $2000000 \text{ cm}^2 \text{ V}^{-1} \text{ s}^{-1}$ with electron densities of approximately $2 \times 10^{11} \text{ cm}^{-2}$ were attained, when a single graphene nanosheet (150 nm) was suspended above a gate electrode composed of Si/SiO₂.

These unique properties of graphene enable it to conduct super-current [67] better than carbon nanotubes or graphite. Graphene's fast and continuous charge carriers, gives it a higher crystal quality and enables it to travel across distances as long as several thousand atoms without scattering [63]. The isolated crystallites of graphene show extraordinary electronic qualities and graphene demonstrates the highest rate of electron motilities as compared to any other possible material giving graphene an upper hand in many applications as electrodes made up of graphene will react faster [63].

Gold nanoparticles have gained popularity in the past few decades as it turned out to be a promising nanomaterial with favorable electrical transport properties for various applications at nanoscale. The synthesis and arrangement of gold nanoparticles in 1,2 and 3 dimensions has resulted in exceptional electrical properties [68], which is caused by Coulomb charging electron transfer supported by molecules and would prove to be beneficial for upcoming microelectronics. However, a vast research is required at the moment to attain reliable results. Moreover, computer models will be required that tolerate any time of defects along with super intelligent software [69], for storage of information and exchange of memory devices to fully exploit the benefits of reliable chemically synthesized nanostructures.

Silver nanoparticles have also gained popularity and attracted an extensive scientific research due to their unique electronic, optical and chemical properties which are dependent on the shape, size, crystallinity, structure and composition of the particles [70]. Silver nanoparticles have been mainly exploited to be used as microelectronic, catalytic, antibacterial and sensor materials [71]. The vast range of applications is due to the unique properties exhibited by silver nanoparticles, such as its melting point which can be reduced drastically due to the fact that the surface energy of these nanoparticles can increase tremendously because of the extreme small size of the nanoparticles [72].

2.5 Recent studies of ZrO₂ nanocomposite

This thesis deals with ZrO₂ nanocomposites so the applications and previous researches regarding this nanocomposite have been studied in detail. Zirconium oxide nanocomposites are available in many forms such as nanofluids, nanodots and nanocrystals. Zirconium oxide nanoparticles are often doped with other composites such as yttrium oxide and magnesia. Zirconium oxide is also known as zirconium, zirconia, zirconic anhydride and zircosol [73].

It is important to know the unique characteristics and properties of zirconia to understand its capabilities. The following table shows selection of chemical properties of zirconia.

Table 3: Chemical properties of ZrO₂ [73].

Property	Chemical data
Chemical symbol	ZrO ₂
CAS No	1314-23-4
Group	Zirconium 4 Oxygen 16
Electronic configuration	Zirconium [Kr] 4d ² 5s ²
Chemical composition	Zirconium 74.03% Oxygen 24.34%

Where CAS No. is a unique number allotted to chemical substances by Chemical Abstract Service (CAS).

Table 4 shows the physical properties of Zirconia.

Table 4: Physical properties of ZrO₂. [73]

Property	Physical data
Density	5680 kg/m ³

Molar mass	231.891 g/mol
Melting Point	2715 °C
Boiling Point	4300 °C

According to the research carried out by W.Chen et al. [74] ZnO₂ nanoparticles having an average particle diameter of 3.1(3) nm are synthesized by means of chemical reaction. ZrO₂ nanocomposites have a cubic structure and the lattice parameter is equal to 4.874(1) Å. The ions of Zn and O are located at the coordinates (000) and (0.413, 0.413, 0.413) respectively. The Zn: O ratio of composition of the nanoparticles is 1:1.9. This cubic structure of ZnO₂ remains stable till 230⁰C under ambient pressure and up to 36 GPa with ambient temperature. ZnO₂ decomposes and breaks down into ZnO when it is exposed to temperatures above 230⁰C. Cubic structured ZnO₂ nanoparticle has a bulk modulus (Bo) of 174(5) GPa and its pressure derivative (Bo') has a numerical value of 4.71. W.Chen, et al. [74] concluded that ZnO₂ nanomaterial belongs to the category of indirect semiconductors and has an energy bandgap of 4.5(5) eV which is paramagnetic down numerically to 5 K.

Vantomme et. al. synthesized a new type of three-length-scaled porous zirconium oxide material with surface area greater than 900 m²g⁻¹ [75]. It has a uniform macroporous structure (300-350 nm) of a supermicroporous, having size of 1.5 nm, nanoparticle approximately 25 nm in size as shown in Figure 19.

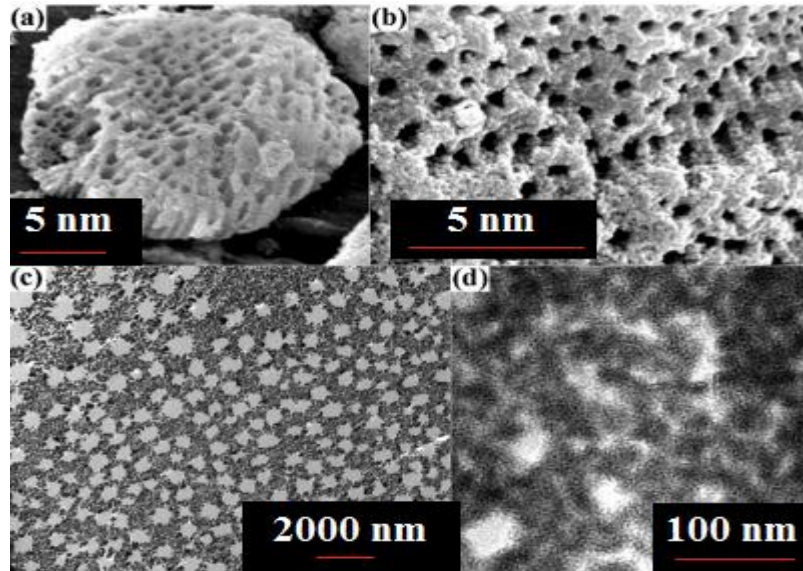


Figure 19: (a,b) SEM image of synthesized zirconium particles displaying uniform macroporosity; (c) TEM image at a low magnification, of a cross section of zirconium highlighting its uniform microporous structure and mesovoids in the wall; (d) TEM image of a region of the microporous wall with high magnification, to show the arrangement of zirconium nanoparticles inside the wormhole like supermicropores having an irregular assembly of mesovoids [75].

These nano-structures have an assembly of irregular mesovoids which are 20-60 nm in the walls having microporous nature as shown in Figure 17. This new material was prepared by one-pot technique and alkyltrimethylammonium was used as a surfactant material [75]. High-surface-area zirconium oxide has significant practical applications in a vast number of fields such as separation and catalysis.

3 Methodology

The famous seminar talk “There’s Plenty of Room at the Bottom”, given by Richard Feynman at the annual meeting of the American Physical Society in 1959 left a huge impact on the development in the field of nanotechnology. In his talk [76], Feynman emphasized that the laws of physics do not act as a barrier in manipulation of nanomaterials. This section deals with the

development in the field of microscopy and the working principles of different types of microscopies available currently.

3.1 Scanning Probe Microscopy (SPM)

Scanning probe microscopy is one of the techniques used for microscopy in which a physical probe is used to scan the surface of sample. In the year 1981, this technique was initiated by the Foundation of Scanning Tunneling Microscope (STM). In STM, the surface topography is measured which generates a map of heights relative to the roughness of the surface. The roughness of topography is measured with the help of tunneling current inside vacuum present between the probe and the conductor [77]. Due to great advancement in the field of semiconductor materials and insulators, a new type of microscope, Atomic Force Microscopy (AFM) was constructed in 1986, which included a small reflective cantilever plate and a photodiode which is discussed in Section 3.2 in more detail. Both STM and AFM proved to be highly beneficial in studying surface properties earned their developers Binnig and Rohrer a Nobel Prize in 1986 [78].

Within the last three decades at least 30 different types of scanning probes devices have been made available which use a different source of information such as noise, light radiation and capacity etc. Each type of microscope measures a specific type of force for example magnetic interaction or electrical forces [78]. Flow chart in Figure 20 shows the general classification of Scanning Probe Microscopy family.

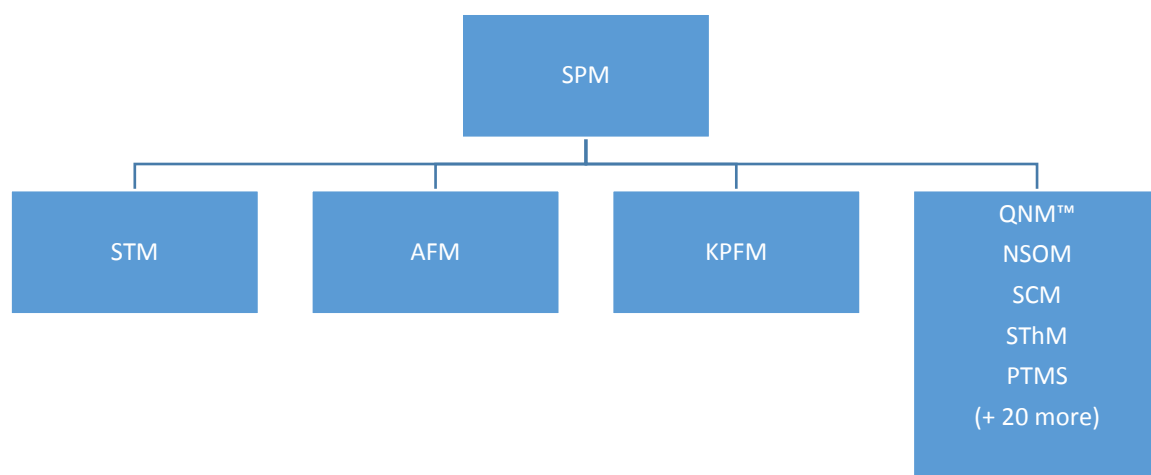


Figure 20: Classification of Scanning Probe Microscopy [78].

It is not possible due to time constraint and the scope of this thesis to discuss all the different types of microscopes so few have been discussed below in detail which serve the purpose of this writing i.e. AFM, KPFM and QNM™.

3.2 Atomic Force Microscopy (AFM)

Atomic force microscopy depends on its ability to sense small forces. A cantilever is present which has a sharp tip and is a means of sensing small forces exerted on the tip by atoms in the sample. To sense and interpret the small forces existing between atoms, it is essential that the cantilever probe is insensitive to any inessential disturbance from the surroundings. These extraneous disturbances are usually caused by sources for instance building vibrations having significant power spectral density in frequency ranging from 0-2 kHz [79]. Hence, to avoid unnecessary effects caused by external disturbances, it is important to keep the resonance frequency of the cantilever greater than 2kHz. However, it is equally important for the cantilever to be sensitive enough to register the interatomic forces.

The forces present between the sample and the tip of the cantilever range from $10^{-7} - 10^{-12}$ N. To achieve deflection greater than 1 \AA for a force equivalent to 10^{-12} N, the value of spring constant (k) of the cantilever should be less than 0.01 N/m [79]. If stiffness is 0.01 N/m and resonance frequency is 2kHz, it indicates a mass less than 10^{-10} kg. These requirements are fulfilled by microcantilevers and they are usually fabricated with silicon oxide and silicon nitride by microfabrication methods. In AFM, the typical dimensions of microcantilevers for length, width and thickness are 100, 10 and 2 μm respectively. However, the stiffness of microcantilevers can fall in the range between 0.06 - 100 N/m [79].

Figure 21 shows a typical setup of AFM. Deflection of the cantilever is measured with the help of a laser beam. The laser beam is made to focus on the cantilever and the beam is reflected from the surface of the cantilever into a split photodiode as shown in Figure 19. The deflection of the cantilever causes a change in the angle between the cantilever surface and the incident laser beam. A change in this angle in turn induces a change in the incidence position on the split photodiode and is recorded as a change in the voltage of the photodiode. The length of the reflected path of the laser is directly related to the cantilever deflection and amplifies it.

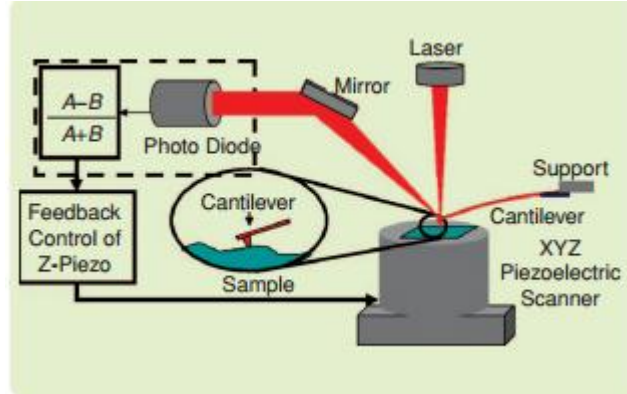


Figure 21: Diagrammatic representation of an AFM setup [79].

As shown in figure, one end of the cantilever is fixed to the base which is typically connected to a dither piezo and the piezo oscillates the base of the cantilever. A scanner stimulated by piezoelectric material helps in positioning the sample in a lateral and vertical direction during the imaging process.

AFM operates in contact, intermediate and non-contact modes. In contact mode, AFM's tip and the surface of the sample touch and the repulsive force between the tip and the sample deflects the cantilever. This deflection is monitored and is utilized as the feedback signal. In non-contact and intermediate mode, the cantilever is oscillated externally close to or at its resonance frequency. The sample-tip interaction varies with the change in distance between them which results in a resonance frequency in non-contact mode and an oscillating amplitude in intermediate mode. The change in amplitude and frequency is used as feedback signal [80] to obtain the topography map of the surface of the sample and is known as Amplitude Modulation (AM) and Frequency Modulation (FM) respectively which are shown in Figure 22.

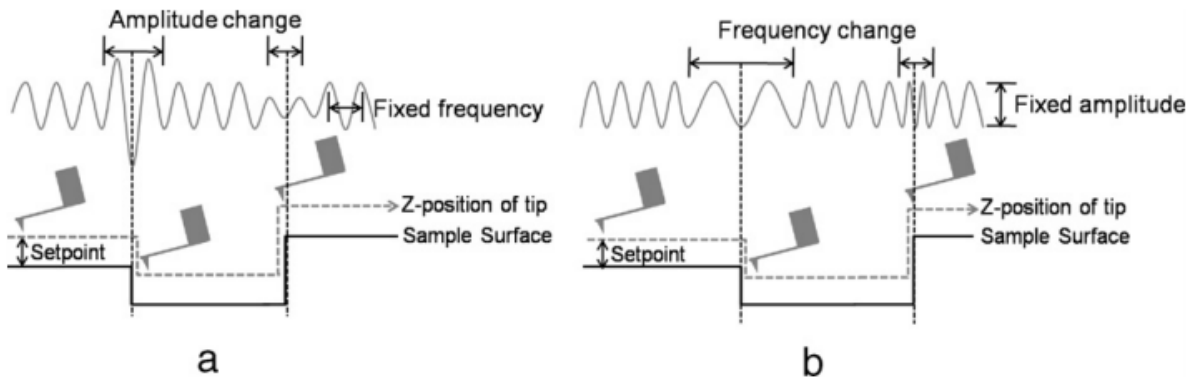


Figure 22: Schematic illustration of non-contact AFM mode: (a) Amplitude modulation mode and (b) Frequency modulation mode [80].

As seen from Figure 22 (a), the amplitude of oscillation increase when the sample-tip distance increases because of decrease in the interaction between tip and sample. The tip-sample is monitored constantly and regulated with the help of feedback system to keep the distance between the tip and sample constant at a point that is pre-determined. Hence, AM mode directly represents the force between the sample and the tip. Figure 22 (b) show FM mode where changes in the frequency of oscillation gives information about the interaction between the tip and sample. Feedback system monitors the change in frequency to keep constant the set-point frequency which is used to map the topography of the sample.

3.2.1 Kelvin Probe Force Microscopy (KPFM)

Kelvin probe microscopy was introduced to measure the amount of local contact difference between the sample and a conducting AFM therefore, KPFM uses the same instrumentation as AFM. KPFM measures contact potential difference (CPD) between the sample and the tip of a conducting AFM. It maps the sample's surface potential or the work function with high spatial resolution. It was first introduced in 1991 by Nonnenmacher et al. [80] and since then KPFM has been used in various methods for characterizing electrical/electronic properties of semiconductor devices or surfaces that are metal/semiconductor in nature.

In high resolution KPFM, short range between the sample and AFM's tip strongly affects CPD. CPD measured with respect to short range force is known as local contact point difference

(LCPD) [81]. It is critical to differentiate between CPD and LCPD while working with KPFM. The CPD, denoted as V_{CPD} , between the sample and the tip is defined by the following equation:

$$V_{CPD} = \frac{\phi_{tip} - \phi_{sample}}{-e}$$

where, ϕ_{tip} and ϕ_{sample} represent the work functions of the tip and sample respectively and e represents electronic charge. When tip of an AFM is brought closer to the surface of a sample, electric force is generated between the surface of the sample and the tip because of the difference in their Fermi energy levels. Figure 22 shows an energy level diagram of the surface of sample and the tip when ϕ_{tip} and ϕ_{sample} are different.

Figure 23 (a) represents diagrammatically the energy levels of the sample's surface and the tip separated by distance d and having no electrical contact between them. When an electrical contact is established, the Fermi levels will get aligned through the flow of the electron current, thus, the system will regain the equilibrium state. Figure 23 (b) shows the case when the sample and the tip are charged establishing V_{CPD} between them, where the Fermi levels remained aligned but vacuum levels are at different levels. Due to this V_{CPD} , electrical force starts acting on the area of contact.

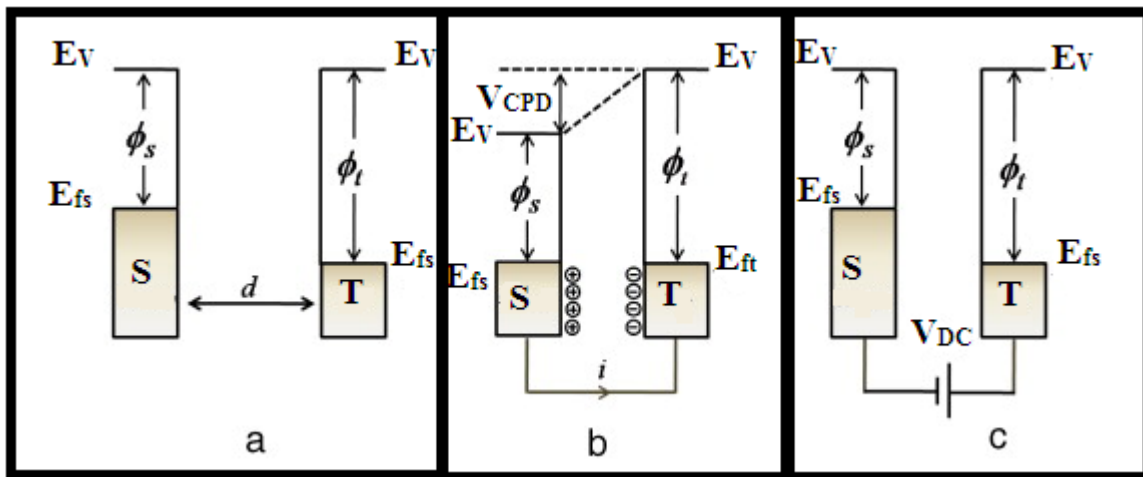


Figure 23: Electronic energy levels of AFM tip (T) and sample (S) for three distinctive cases: (a) sample and tip are separated by a distance ' d ' and have no electrical contact; (b) sample and tip in an electrical contact; (c) an external bias (V_{DC}) is applied between sample and tip to

invalidate the CPD and thus the electrical force between tip and sample (E_v shows the vacuum energy level, E_{ft} and E_{fs} represent the Fermi energy levels of the tip and the sample respectively) [81].

Figure 23 (c) demonstrate that the electrical force on the contact area can be nullified. When an external bias (V_{DC}) is applied, it has the same magnitude as that of the V_{CPD} but in opposite direction. This voltage will eliminate the surface charge present in the contact area. The amount of external bias (V_{DC}) that reverses the electrical force caused by V_{CPD} is equivalent to the work function difference between the sample and the tip. Hence the work function of the sample can be calculated provided the tip work function is given. Work function of the sample can be measured by KPFM when AC voltage (V_{AC}) plus DC voltage (V_{DC}) is applied to the AFM tip. Oscillating electrical forces are generated between the AFM tip and sample by V_{AC} , and V_{DC} nullify the oscillating electrical forces caused by CPD between the sample's surface and the tip of AFM. Electrostatic force (F_{es}) between the sample and the tip is given by:

$$F_{es}(z) = -\frac{1}{2}\Delta V^2 \frac{dC(z)}{dz}$$

Where z represents the direction perpendicular to the surface of the sample, ΔV is the value of potential difference between the voltage applied to the tip of AFM and V_{CPD} , and dC/dz shows the gradient of capacitance between sample's surface and tip. If $V_{AC} \sin(\omega t) + V_{DC}$ is applied across the tip of AFM, the voltage difference (ΔV) is calculated by:

$$\Delta V = V_{tip} \pm V_{CPD} = (V_{DC} \pm V_{CPD}) + V_{AC} \sin(\omega t)$$

Where, "±" sign depends on where the bias (V_{DC}) is applied; if it is applied to sample it is + and if it is applied on tip it is -. Substituting ΔV into $F_{es}(z)$ results in the electrostatic force applied to the AFM's tip which is as follows:

$$F_{es}(z, t) = -\frac{1}{2} \frac{\partial C(z)}{\partial z} [(V_{DC} \pm V_{CPD}) + V_{AC} \sin(\omega t)]^2$$

The expression obtained for $F_{es}(z, t)$ can divided into three sub equations;

$$F_{DC} = -\frac{\partial C(z)}{\partial z} \left[\frac{1}{2} (V_{DC} \pm V_{CPD}) \right]^2$$

$$F_{\omega} = -\frac{\partial C(z)}{\partial z} (V_{DC} \pm V_{CPD}) V_{AC} \sin(\omega t)$$

$$F_{2\omega} = \frac{\partial C(z)}{\partial z} \frac{1}{4} V_{AC}^2 [\cos(2\omega t) - 1]$$

F_{DC} gives the amount of static deflection of the AFM's tip, F_{ω} is used to measure the value of V_{CPD} where ω is the frequency and $F_{2\omega}$ is used in capacitance microscopy.

For semiconductor surfaces, F_{ω} is calculated by:

$$F_{\omega} = -\frac{Q_s}{\epsilon_0} \frac{C_I C_D}{C_I + C_D} V_{AC} \sin(\omega t)$$

Where Q_s represents the total amount of charge present near the semiconductor's surface due to surface potential, ϵ_0 represents the dielectric constant, C_I is capacitance related to the air gap between sample and tip and V_{AC} , and C_D is the capacitance related to V_{AC} and space-charge-layer (SCL) on the surface of a semiconductor.

KPFM can operate in Frequency Modulation (FM) and Amplitude Modulation (AM) modes just like AFM can be used to detect atomic forces by both modes. The electrostatic force denoted by F_{ω} can be detected by both modes in KPFM. In AM mode, KPFM directly measures F_{ω} from the amplitude of the oscillation of the cantilever (ω) that is induced by V_{AC} and V_{CPD} . When V_{DC} is applied to the tip of the AFM to nullify the amplitude that is measured it also measures V_{CPD} . However, in the FM mode, KPFM detects the shift in frequency at ω and to nullify the shift in frequency, V_{DC} is applied to the tip of the AFM which measures V_{CPD} .

KPFM measures both V_{CPD} and topography side by side with the help of AFM tip. Therefore, it is essential to have a strategy to separate V_{CPD} from the topographical signal. In an experimental setup for KPFM to avoid any cross-talk between CPD measurement and the topography signal, modulation is carried out in V_{AC} at a frequency that is higher than the bandwidth of the feedback

system of topography [81]. In KPFM AM mode, the topography is measured by tracking the oscillation at the first resonance frequency of the tip of AFM, whereas V_{CPD} is also measured by amplitude of the oscillation but at the AFM tip's second resonance frequency. However, the amplitude of the second resonance peak is numerically less than one-third of the peak of the first resonance frequency. The second resonance peak's frequency is 6 times the frequency of the first resonance peak [82]. To excite the tip of AFM by means of electrical force, the V_{AC} is tuned to the second resonance frequency whereas the first resonance frequency is used to control the height of the tip. These strategies help to segregate the signals of topography and V_{CPD} . In a converse manner, in FM mode of KPFM, the tip of AFM is excited mechanically with the help of first resonance frequency. V_{AC} helps in inducing a modulation in the electrostatic force and this modulation is detected by the superimposed oscillation due to the frequency variation of the AFM tip's mechanical oscillation [82]. This enables to separate the signal of V_{CPD} and topography.

Figure 24 shows the schematic diagram of an experimental setup of KPFM. The lower part of the schematic diagram demonstrates the FM mode of AFM system to measure topography whereas the upper part is composed up of components required to carry out CPD mapping and include lock-in amplifier and KPFM controller. The bold straight lines and the dashed lines in the diagram demonstrate the FM and AM modes KPFM respectively. V_{AC} is applied to the AFM tip via lock-in-amplifier reference signal voltage output (OSC_{out}) [81]. In the FM mode, frequency shift signal shown as Δf is split into two signals; one signal is fed into the z regulator to perform topographic imaging and the other signal is sent to the lock-in amplifier. The lock-in amplifier helps in the extraction of the signal that has the same frequency as V_{AC} and then feeds this signal to the KPFM controller. The KPFM controller maintains the feedback system which nullifies the lock-in output signal by the application of V_{DC} to the tip. In contrast, in AM mode, V_{AC} having the same frequency as the second resonance peak of the oscillation of the tip is applied to the tip of AFM to cause excitation in the tip with the help of electrical force.

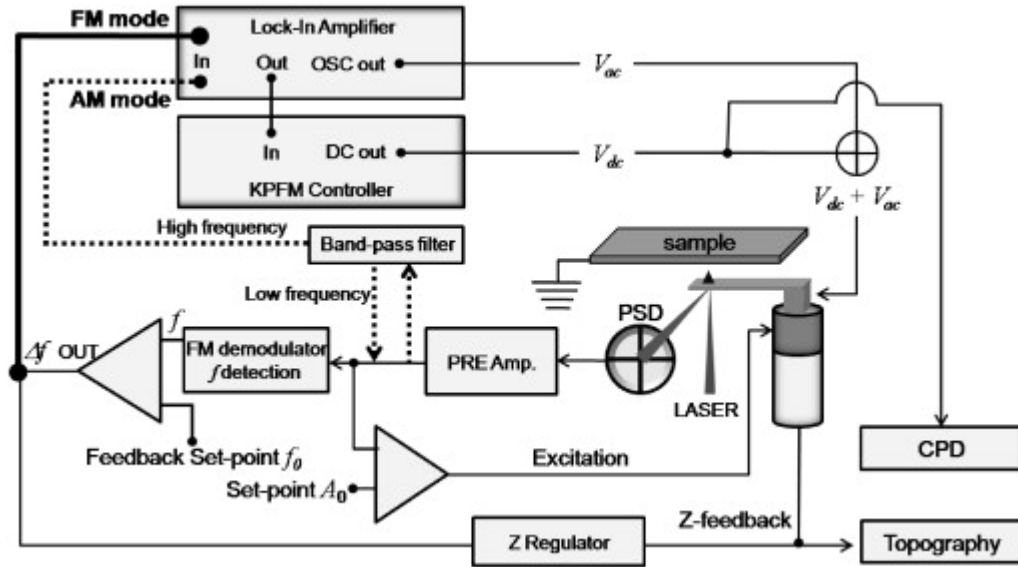


Figure 24: Schematic diagram of KPFM system showing AM and FM modes separately. Lower part is FM mode AFM system to carry out topography imaging and upper part shows KPFM system to measure CPD [81].

The KPFM controller that is measuring CPD uses the second resonance frequency component. It is critically important to prepare conducting and atomically sharp AFM tips for high-resolution KPFM.

3.2.2 Quantitative Nanoscale Mechanical Property Mapping (QNM™)

Peak Force QNM™ was released by Veeco in 2010 and it made it possible to reduce the need of utilizing special probes. Peak force QNM works on the principals of Veeco’s Peak Force Tapping™ technology for the feedback system. It is possible to conduct high-resolution mapping of mechanical properties keeping number of pixels and scanning speeds similar to Tapping Mode. Analysis of the data collected from the force curve can be done on the fly which provides a map of several mechanical properties. The resolution of the map and the height of image are same. This feature has helped in minimizing the loss of resolution due to larger area of tip-sample contact by limiting the sample deformation depths to a few nanometers [83]. Moreover, Peak Force Tapping also provides the possibility to directly control maximum normal force, as a result the deformation depth of the sample can be controlled and any lateral forces are eliminated. This serves as a protection for both the sample and the tip. Another important

benefit of using Peak Force Tapping is achieving unambiguous quantitative data for a wide range of materials due to availability of many different probes. Broad range of adhesion or modulus properties can be covered while excellent signal-to-noise ratios are maintained. The entire force curve can be analyzed for each single tap allowing independent measurement of different properties [83].

Peak Force QNM™ uses force-volume technique and the speed with which the curves for force can be attained is increased significantly i.e. at 1 or 2 kHz. A complete force curve is generated for each pixel in the image which results in a large time required to receive the data [84]. QNM™ mode has been recently introduced, hence a limited number of scientific publications is available for it.

Force-time curve achieved from QNM™ is displayed in Figure 25 where B is the contact point of the probe and the sample, C is the peak force and D shows the adhesion.

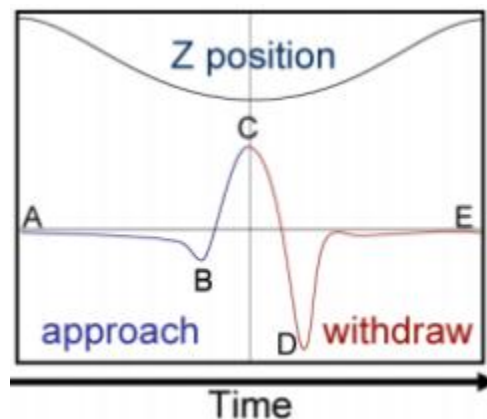


Figure 25: One cycle of QNM™ mode or (Force vs Time curve) [85].

The blue part of the curve shows the approaching of the tip towards the sample and the red part indicates retract. The information of z-position is used to convert the heartbeat into force curve plot which is analyzed to produce the peak force to create a control feedback signal and the sample's mechanical properties such as modulus, adhesion, dissipation and deformation at nano-scale etc [85]. These properties can be used in future to study the impact of humidity on

electric potential. Such as the map of adhesion can be generated by areas on the sample where charge is accumulated, and this can give us additional detailed insight into the relationship between humidity and electric potential.

4 Experimental Components and Procedure

This section deals with the components used in the experimental setup in detail regarding the working principles, how and why they were chosen. Moreover, final experimental setup is discussed along with the challenges faced during the establishment of the setup.

4.1 Sensors

Humidity accounts for the presence of water molecules in air. Most manufacturing processes work best under a certain range of humidity and are effected by the amount of water vapours present in the surrounding atmosphere. Water vapour can also influence a variety of chemical, biological and physical processes. Hence, the measurement of humidity is a critical requirement, because it may have a direct or indirect impact on final cost of products and health of people working in a humid environment. [86].

The most common units to measure humidity are Dew/Frost point (D/F PT), Relative Humidity (RH) and Parts Per Million of water molecules in gas (PPM) [87]. RH is a relative measurement and indicates humidity as a function of temperature. While D/F PT is in relation with gas pressure, however, it is independent of temperature. This makes D/F PT an absolute term like PPM. Figure 26, shows the relation between these units.

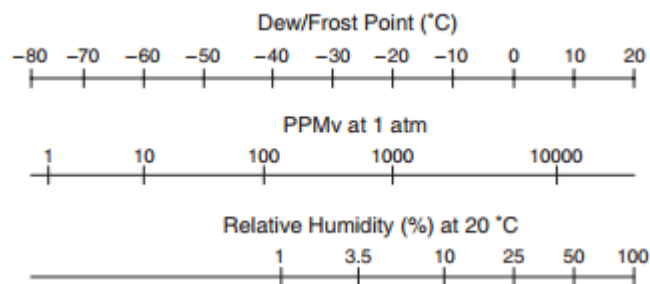


Figure 26: Co-relation between Relative Humidity, Dew point and Parts Per Million of water molecules in gas at 1 atm [87].

Measurement of humidity helps in determining the amount of water vapor present in a gaseous state which may be a type of mixture, for instance air, or it may be some pure gas for example argon or nitrogen. There are various terms commonly used to indicate the humidity level as tabulated in Table 5.

Table 5: Various terminologies used to indicate the level of moisture [86].

No.	Term	Definition	Unit
1	Absolute Humidity (Vapor Concentration)	Ratio of mass (vapor) to volume.	grams/m ³
2	Mixing Ratio or Mass Ratio	Ratio of mass (vapor) to mass (dry gas).	grams/m ³
3	Relative Humidity	Ratio of mass (vapor) to mass (saturated vapor) or ratio of actual vapor pressure to saturation vapor pressure.	%
4	Specific Humidity	Ratio of mass (vapor) to total mass.	%
5	Dew Point	Temperature (above 0 °C) at which the water vapor in gas condenses to liquid water.	°C
6	Frost Point	Temperature (below 0°C) at which the water vapor in a gas condenses to ice.	°C
7	Volume Ratio	Ratio of partial pressure (vapor) to partial pressure (dry gas)	% by volume
8	PPM by Volume	Ratio of volume (vapor) X 10 ⁶ to volume (dry gas)	PPM _v
9	PPM by Weight	PPM _v X	PPM _w

In this experiment five sensors were used to check the relative humidity level. One analog Honeywell HIH-4040 humidity sensor and 3 different types of digital humidity sensors: Vaisala, KIMO and two Humidity sensors DHT 11. Three humidity sensors were available for the experiment i.e. Honeywell HIH-4040 humidity sensor and two DHT-11 sensors. However, all three sensors were wrongly calibrated so two other humidity sensors, Vaisala and KIMO, were

borrowed from LUT Chemistry Department to compare and chose the best sensor to calibrate our three sensors and later choose the best among Honeywell HIH-4040 and the two DHTs. The accuracy of all five sensors is shown in Table 6.

Table 6: Specifications of sensors used in experiment.

Sensor	Relative Humidity % RH	Temperature °C	Accuracy Relative Humidity % RH	Accuracy Temperature °C
KIMO VT 210: Probe SMT 900	5 - 95	-20 – 80	± 1.8	± 0.3
Vaisala HMI 41: Probe Vaisala HMP46	0 - 100	-40 – 100	± 2.1	± 0.3
DHT11 (4 pin)	20 - 90	0 – 50	± 5	± 2
Honeywell HIH-4040	0 - 100	-40 – 85	± 3.5	-

In order to get the accurate readings, the sensors had to be calibrated according to some reference sensor. Initially, KIMO was considered as the reference as it is a highly-sophisticated apparatus and enjoys a wide range of suitable operational conditions. Moreover, KIMO was recently calibrated in January 2016 Department of Chemistry (LUT), however later it was decided not to use it as reference as it was found to be uncalibrated and failed to give accurate readings when it was compared to the controlled environmental conditions in paper room (LUT) where the conditions are maintained at 23 ± 1 °C and relative humidity of 50 ± 2 % whereas KIMO was showing RH value of 68.6% as shown in Figure 27.



Figure 27: Controlled environmental conditions in paper room 2153 (LUT) and readings displayed by KIMO sensor.

Relative humidity and temperature were measured in different environmental conditions using all five sensors as shown in Table 7.

Table 7: Relative humidity and temperature measured in various environments.

Environment	HIH-4040	DHT11 -1		DHT11 -2		Vaisala HMI 41		KIMO VT 210	
	RH(%)	T(°C)	RH(%)	T(°C)	RH(%)	T(°C)	RH(%)	T(°C)	RH(%)
AFM Room (1037)	39	19	21	19	33	19.4	25	19	47
SEM Room (2443B)	34	21	22	22	33	21.1	23.3	21.2	48.2
Saimaa Restaurant	45	20	33	21	39	20.1	21.8	21.4	58.3

Street (26.10) 1 ^o C / 95%	68	9	29	10	40	6.8	55	2	82
Paper Room (2153)	57	23	42	24	43	23	49	23.2	68.6
Paper Lab. TH-KE-100 system (2152)	86	21	57	21	62	23	75	–	–
Wet napkin	117	15	95	16	93	19	96	19	100
Air-line-AFM Room (1037)	15.5	19	21	19	32	18.8	5.5	18.8	24.8
Air-line SEM (2443B)	8	23	19	23	28	23.5	2	23.9	20
Liquid Nitrogen AFM Room (1037)	7.7	19	21	19	32	–	–	–	–
Nitrogen line- SEM Room (2443B)	6	22	19	22	29	23.3	0.4	25.8	17

The values were used to construct graph shown in Figure 28 to compare and choose the most suitable reference sensor. X-axis shows the true humidity values and y-axis shows the readings obtained by the other humidity sensors to choose the best candidate to be used as reference to calibrate Analog HIH and DHT-11 sensors.

Only those readings of each sensor were used to construct the graphs which lied inside the operating range of the sensor to exclude the wrong values obtained due to the limitations of the sensor.

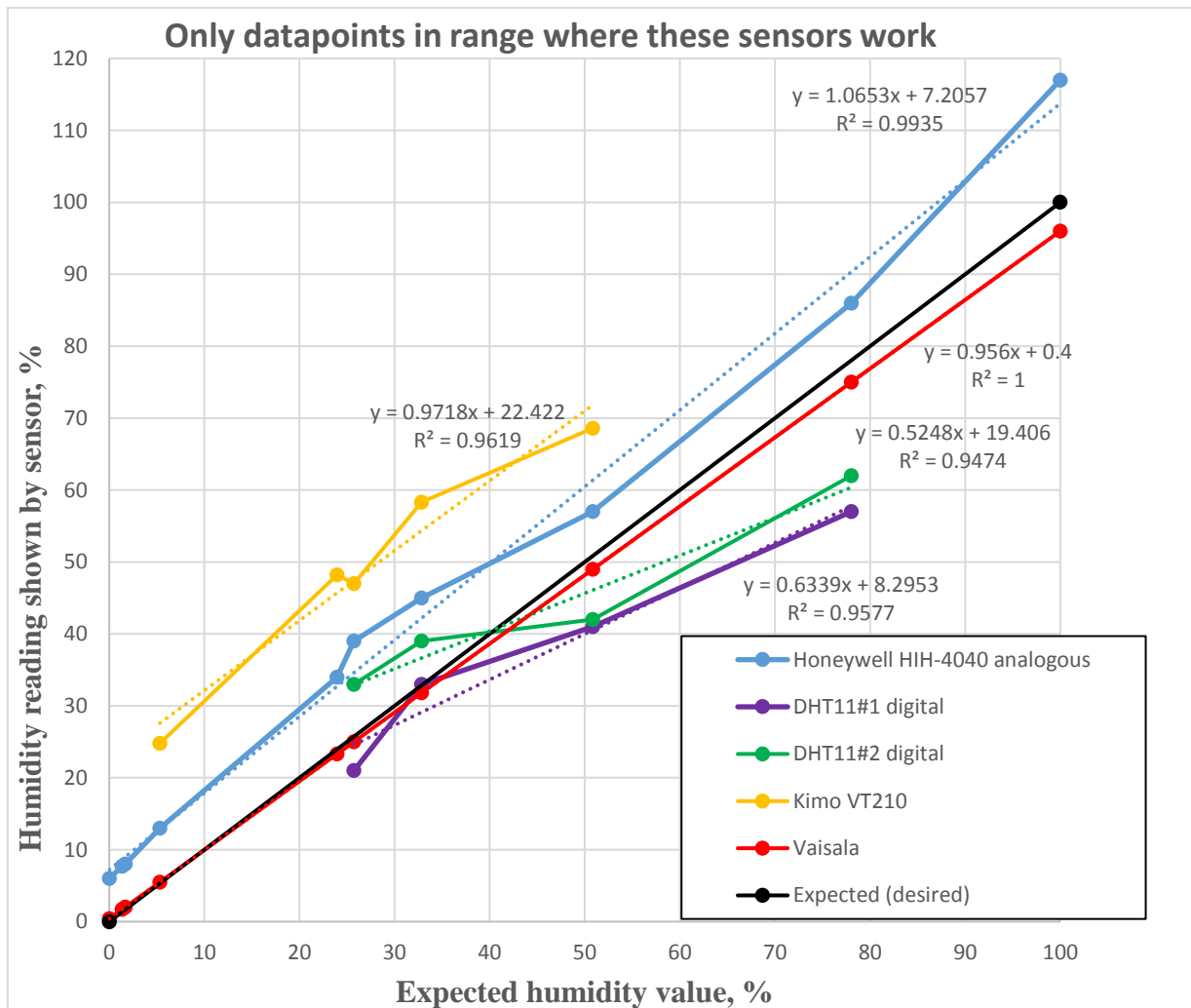


Figure 28: Comparison graphs of all available humidity sensors with respect to expected humidity values to choose the best humidity sensor.

The graph of expected humidity was drawn as a linear graph between coordinates (0, 0) and (100, 100) which signifies that when the humidity is 0 % and 100 % the reading shown by sensor is 0 % and 100 % respectively. As shown in the Figure 28, Vaisala sensor graph trend mimics the expected value trend line most successfully, hence it was chosen as the reference sensor to calibrate the three other sensors used for the experiment: analog HIH-4040, DHT11-1 and DHT 11-2. Figure 28 also shows the equation of each trend line and the coefficients in each equation were used to recalibrate the sensors by adding these coefficients in the code mentioned in Section 4.3 in order to program the Arduino Uno to connect humidity sensor.

The graph also clarified that among analog HIH-4040 and the two digital DHT 11 sensors, HIH-4040 was most accurate to be relied on for the experimental measurements as it had shorter response time and the measurement values were repeatable and more accurate compared to DHT 11. It was also chosen because the operating range of HIH-4040 is wider as compared to the digital sensors hence all microscope readings were carried out by using Honeywell HIH-4040 as the humidity sensor.

4.1.1 Working principle and type of Humidity Sensors

Relative humidity sensors are composed up of thermoset polymer, platinum electrodes, three layered construction of capacitors and silicon chip on which voltage output signal conditioning is integrated as shown in Figure 29.

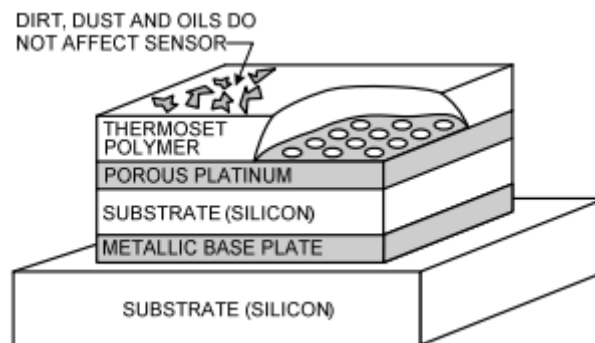


Figure 29: Construction of Relative Humidity Integrated Circuit (RHIC) sensor [88].

During operation, water vapour present in the dielectric layer of the active layer reaches equilibrium with the surrounding gas. The platinum layer, which is porous in nature, acts as a shield for the dielectric response from any external influences. The protective polymer present over the layers gives protection to the platinum layer against contaminants such as dust, dirt and oil. A heavy layer of contaminants may slow down the response time of the sensor as the time required for water vapour to reach equilibrium in the sensor [88].

The output of humidity sensors that absorb water vapour depends on both percentage of relative humidity and temperature. The linear voltage output of Relative Humidity Integrated Circuit (RHIC) sensor is a function of % RH, V_{SUPPLY} and temperature. As the voltage supply increases,

there is an equal proportional increase in the output voltage and follows two set of equations as stated below.

$$\% \text{ RH} = (V_{\text{OUT}} / V_{\text{SUPPLY}} - 0.16) / 0.0062$$

$$\text{True RH} = (\% \text{RH}) / (1.0546 - 0.00216 T)$$

Where T is measured in °C. Condensation can occur when the temperature of the surface of the active area of the sensor drops below the value of ambient dew point of the gas surrounding the sensor. Condensation can occur even when the surface temperature drops minutely below the ambient dew point. Small fluctuations in temperature can cause condensation when working with humidity level above 95 %. Although it takes little time for water to condense, evaporation of water is a relatively slow process during high humid conditions which corresponds to surface temperature of sensor being only slightly more than the ambient dew point. Hence, the recovery period of a sensor from wetting is longer compared to the normal response time of the sensor. During recovery, the sensor shows a constant output of 100 % RH irrespective of the ambient RH [88].

Humidity sensors are broadly categorized into capacitive and resistive type. Humidity sensors that rely on the principles of capacitive effect, are composed up of hygroscopic dielectric material which is present between a pair of electrodes. This forms a small capacitor. Majority of capacitive type humidity sensors use polymer or plastic as the dielectric material and the dielectric constant ranges from 2 – 5. When no humidity is present, the value of capacitance is determined by the geometry of the sensor and the dielectric constant of the hygroscopic dielectric material. At room temperature, water vapour has a dielectric constant of approximately 80 which is larger than the dielectric constant of the hygroscopic dielectric material. As a result, water is absorbed by the sensor due to concentration gradient and in turn increases the value of capacitance of the sensor. During equilibrium conditions, the amount of water vapour that is present in the hygroscopic material depends not only on the pressure of ambient water vapour but also on the ambient temperature. Relative humidity depends on water vapour pressure and ambient temperature. Hence, relative humidity, the amount of moisture in sensor and the sensor capacitance are dependent on each other and this relationship controls the

operation of the capacitive humidity sensor [86]. Figure 30 shows a general structure of a capacitive type humidity sensor.

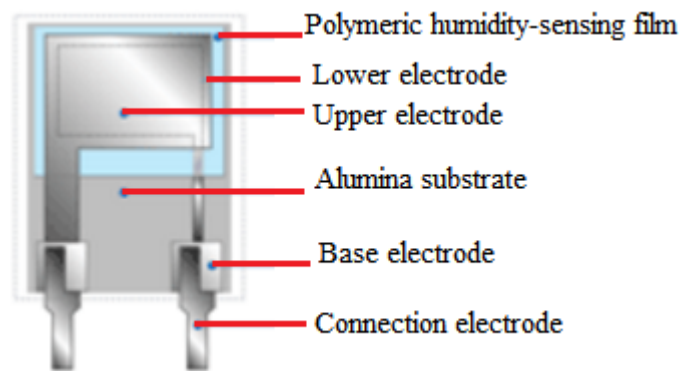


Figure 30: General layout capacitive type humidity sensor [86].

Substrate is made up of Alumina and the lower electrode is made from platinum, gold or some other material. A layer of polymer e.g. Polyvinyl-Alcohol (PVA) is deposited on the electrode which is capable of sensing the amount of humidity. A layer of gold is deposited on top of the polymer layer which operates as the top electrode. Additionally, the top electrode functions as a pathway for water vapour to pass through it and enter the sensing layer. The movement of water vapour through the hygroscopic sensing layer continues until equilibrium is reached between the amount of vapour in sensor and the vapour in gas or ambient air. Hence, a capacitive type sensor is a capacitor which has a thin film of humidity sensitive polymer as its dielectric material [86].

The second type of humidity sensors are based on the resistive effect. Resistive type humidity sensors sense the change in the value of resistance of the sensor element with respect to humidity. Figure 31 shows the general structure of a resistive type humidity sensor.

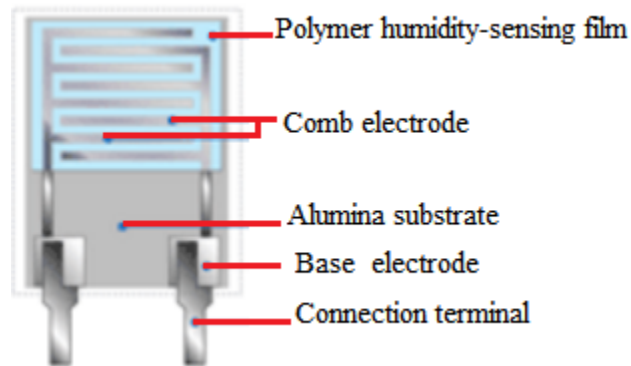


Figure 31 General layout of resistive type humidity sensor [86].

A thick film of a conductor material like ruthenium oxide and gold is printed and then calcinated in the form of a comb in order to form the electrode. A layer of polymeric electrode is applied and this film senses humidity due to the presence of mobile ions. Change in the number of mobile ions causes a change in the impedance [86].

4.2 Soldering wires and connecting wires to mother board Arduino Uno

In order to prevent unfair humidity readings due to lose contacts, the wires were soldered together using Weller WD1 soldering iron system as shown in Figure 32 (a) whereas (b) shows the specifications of soldering wire used.



Figure 32 (a) Weller WD1 soldering iron system b) tin/lead soldering wire.

The soldering iron was heated to 275 °C. 60/40 tin/lead alloy soldering wire was used to melted to form firm soldered connections between the wires and the connecting header male pins which were then connected to the Arduino Uno as shown in Figure 33.

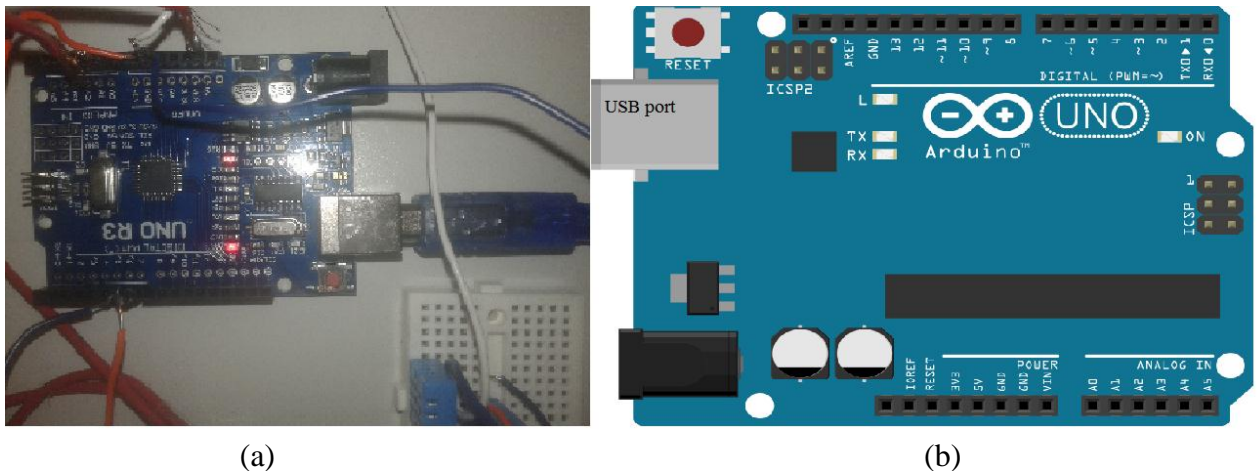


Figure 33: a) Soldered wires connected to Arduino Uno board into respective ports b) general layout of Arduino Uno board [89].

The male header pins soldered to wires were connected to the Arduino Uno in the following way:

Analog HIH -A0

DHT 1 signal pin- pin 6

DHT 2 signal pin -pin 7

Ground wire connected to GND pin

5 V - VIN

4.3 Software code

The DHT Lib and following example code was copied from Circuit Basics [90] to install the software code to initiate the sensing process of DHT1, DHT2 and Honeywell HIH-4040 via Arduino. The example code was modified to meet our requirements and to recalibrate DHT1

and DHT 2 as they were showing false readings due to wrong calibrations using the coefficients of equation achieved in Figure 27. Moreover, help was taken from YouTube tutorial video [91] to follow the procedure to correctly set up DHT11s and include Honeywell HIH-4040 on Arduino so all humidity readings are displayed on the PC monitor.

```
#include <dht.h>
dht DHT1;
dht DHT2;

#define ANALOG_PIN A0
#define DHT1_PIN 6
#define DHT2_PIN 7

//float ANALOGSTEP = 3. / 1024; // MAXOUTPUT VOLTAGE = 5V * 0.7952 = 3.976V
int chk1 = 0;
int chk2 = 0;
int analogSens = 0;
void setup(){
  Serial.begin(9600);
}
void loop()
{
  chk1 = DHT1.read11(DHT1_PIN);
  Serial.print("T1 = ");
  Serial.print(DHT1.temperature);
  Serial.print("; H1 = ");
  Serial.print((DHT1.humidity)*10/6 - 13);
  chk2 = DHT2.read11(DHT2_PIN);
  Serial.print(" | T2 = ");
  Serial.print(DHT2.temperature - 3);
  Serial.print("; H2 = ");
  Serial.print((DHT2.humidity)*19/10 - 39);
  analogSens = (analogRead(ANALOG_PIN)/1024.0) * 5 * 30.28073 - 32.5705;
  Serial.print(" | AH = ");
  Serial.println(analogSens);
```

```
delay(3000);  
}
```

4.4 Setting variable environmental conditions

One important parameter of this entire experiment was to establish a controlled humidity control system capable of varying the value of relative humidity. In order to ensure controlled conditions around the sample, a gas cell was utilized shown in Figure 34. This enabled the use of AFM methodology.

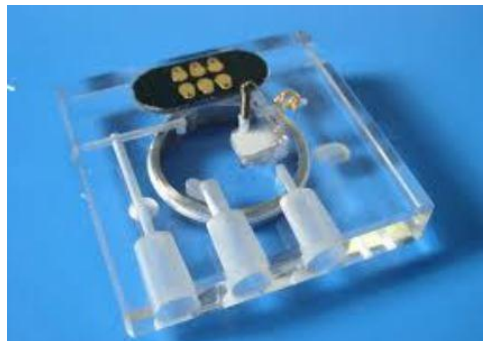
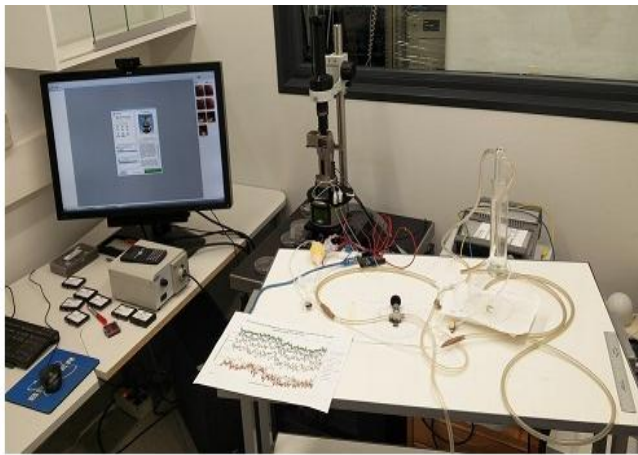


Figure 34: Gas cell image

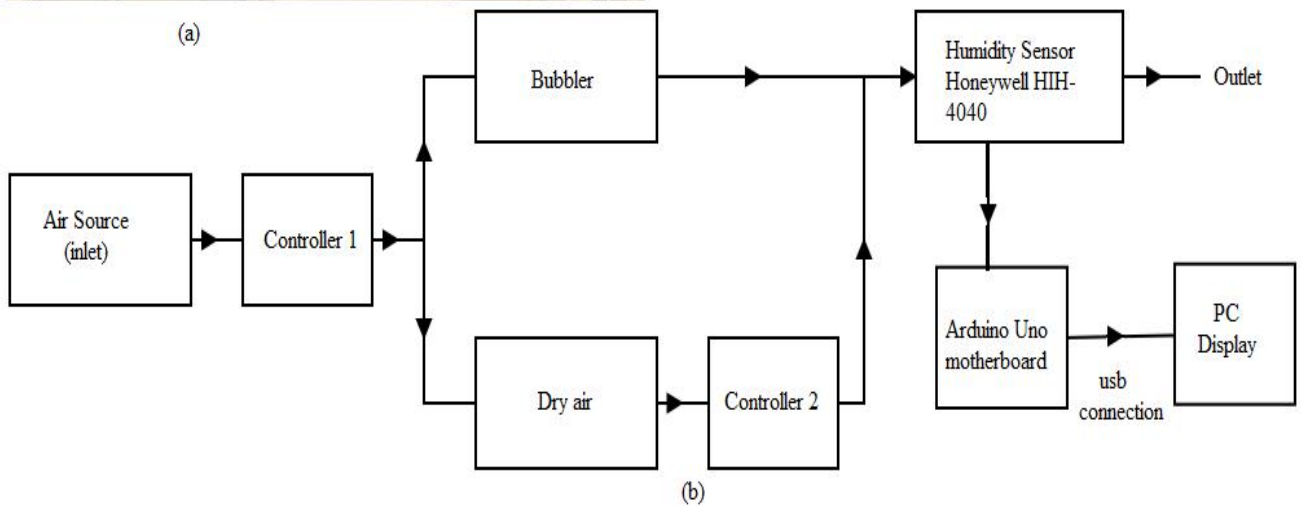
Silicon rubber seal holds the gas cell together and acts as a sealant to create controlled atmospheric conditions inside the gas cell. Due to a need of optical transparency and low thermal coefficient, the body of gas cell is composed up of transparent silica fused together. To carry out experiments in variable atmospheric conditions, a humidity control system was set up. Final setup and schematic diagram of the controlled humidity set up is shown in Figure 35 (a) and (b) respectively and is composed up of following components:

1. Air source inlet
2. Controller 1 (Air source controller)
3. Bubbler
4. Bypass valve
5. Dry air
6. Controller 2 (dry air controller)
7. Humidity sensor (Honeywell HIH-4040)

8. Gas cell
9. Outlet
10. Arduino Uno motherboard
11. Usb hub
12. PC display



(a)



(b)

Figure 35: (a) Final experimental setup (b) Schematic diagram of humidity control system.

Water vapors are essential to increase the level of humidity. In order to create the desired level of humidity, the bypass valve and the outlet valve are kept open for few minutes. The valves are closed when the humidity sensors indicated the value of desired humidity level inside the

system. However, while taking actual measurements, the valves are kept close to ensure that atmospheric humidity has minimum influence on the tip of AFM's probe.

Here we need to remind that Vaisala was only used to calibrate our humidity sensor, Analog Honeywell HIH-4040, which was used to measure the value of humidity throughout the electric potential measurements. Linear voltage output produced by Honeywell was measured by multi-meter available in laboratory. It operates on supply voltage of 4.5 V [92] which was taken from batteries. The electrical schematic diagram of HIH sensor as shown in Honeywell-4000-02 datasheet is given in Figure 36.

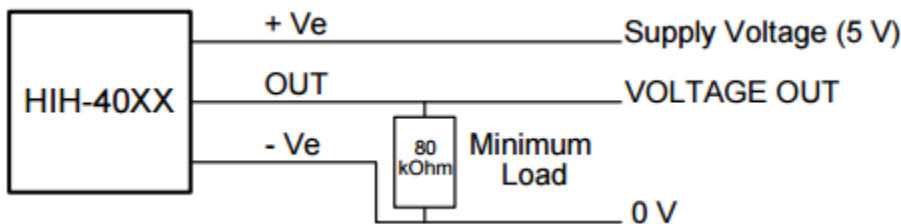


Figure 36: General application circuit of Analogue Honeywell HIH-4000-02 [92].

According to datasheet, Honeywell HIH-4000-02 [92] has following specifications: a relative fast response of five seconds, a small hysteresis and an overall accuracy of 3.5%. The recommended operating temperature range is specified to be between -40 and 85 °C which includes the range needed to carry out the experiment. The humidity control system was able to provide controlled humidity level inside the gas cell within a range of 0 and 100% \pm 3%.

In order to achieve different values of humidity, the pressure inside the system was kept constant by keeping angle of openness of controller 1 (air source) at a fixed position and the degree of openness of dry source was changed to vary the number of bubbles produced in water bubbler hence to change the humidity level inside the system. Lower degree of openness of dry valve correlates with lower humidity. The amount of bubbles varies, but the overall pressure stayed constant throughout the closed system and in the measurement chamber of the AFM. For each

change in the openness of the dry valve, both the highest value of humidity and the final value of relative humidity after 20 minutes were tabulated. These values were used to form graph to find the relationship between the openness of the dry valve and the humidity to create a controlled humidity system. The graph obtained is shown in Figure 37.

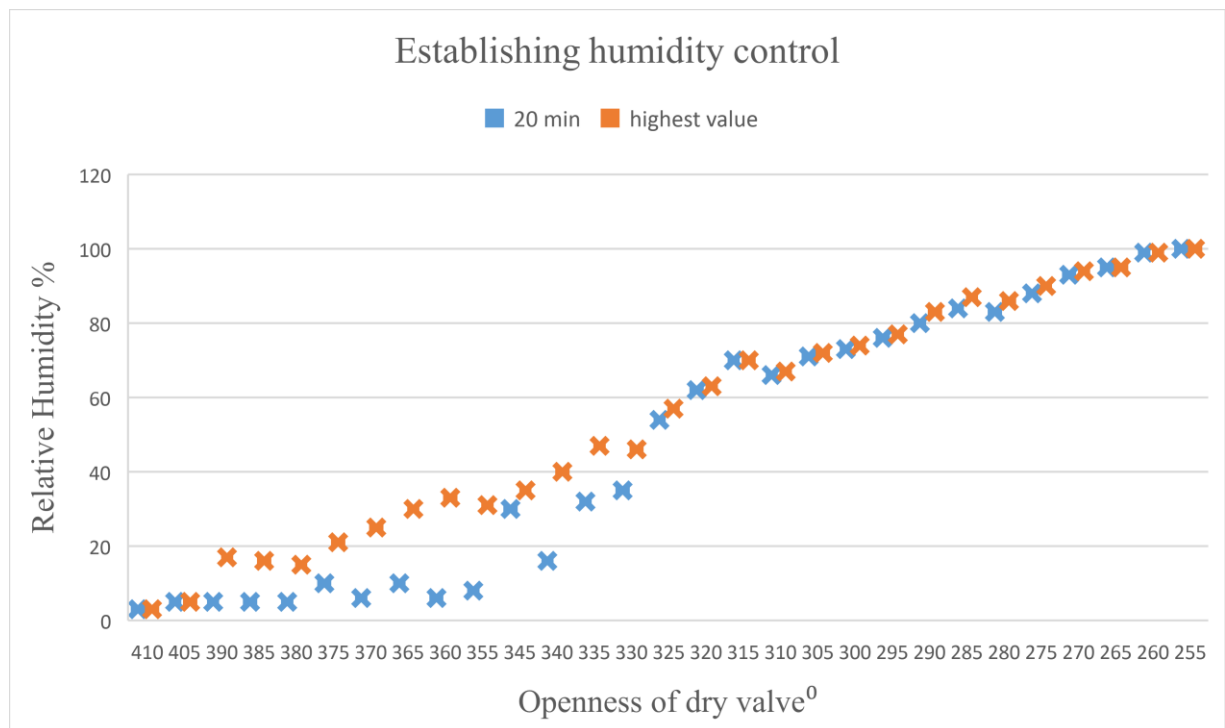


Figure 37: Graph of Relative humidity with respect to the openness of dry valve to establish controlled humidity (lower degree of openness of dry valve correlates with lower humidity).

Y-axis contains the value of relative humidity in % and x-axis have the openness of the dry valve in degrees. The blue data points refer to the value of relative humidity achieved after 20 minutes and orange data points depict the highest value of relative humidity achieved for each angle of the dry valve. The readings were started by completely opening the dry valve at 410° and the value of relative humidity was smallest as all air from the air source was passing through the dry source pathway instead of the bubbler filled with fixed volume of water. This is because the dry air pathway provided the least resistance to air flow because it was open. As the dry valve was closed, more air passed through the bubbler and absorbed moisture from the water

inside. This explains an increase in humidity with a decrease in the angle of openness of the dry valve. Finally, 100% humidity was achieved when the dry valve was at 255° .

5 Measurements

A specific area of $4\mu\text{m}$ by $4\mu\text{m}$ was chosen on the sample shown in Figure 38 to carry out all measurements.

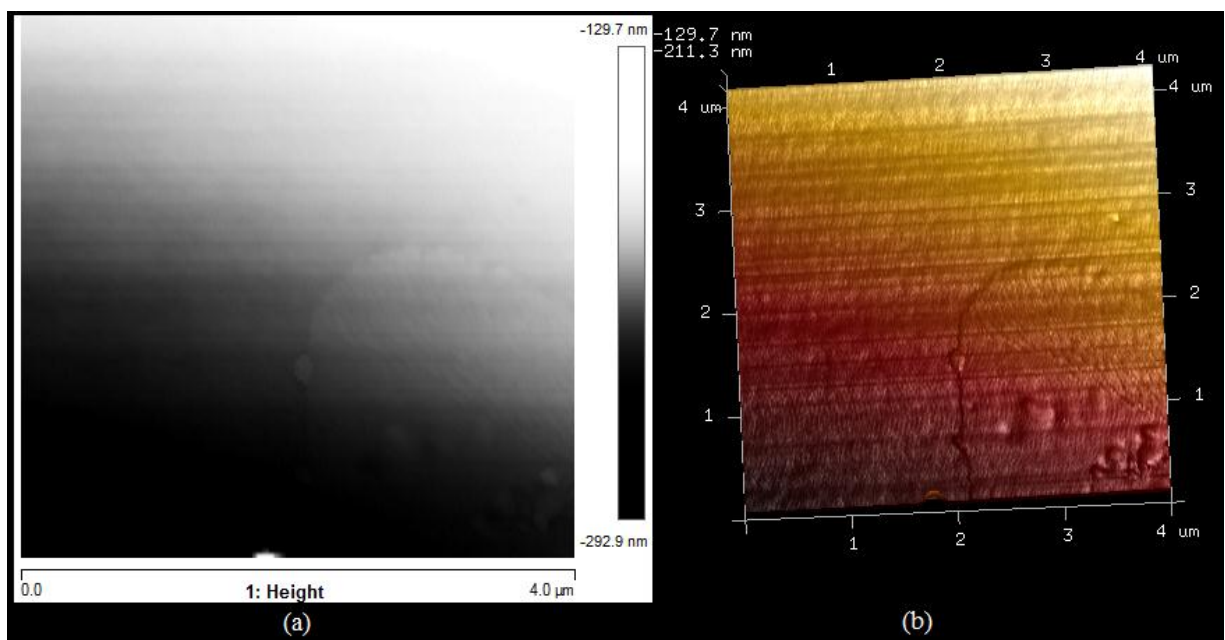


Figure 38: Chosen area of the sample a) 2D cross- section and b) 3D image of the same area.

Extreme care was taken during experiments to ensure that each reading was conducted for the same site to ensure fair comparison between the electric potential values achieved for each humidity condition.

Not only the end of the tip of the probe and the sample influence the relative electrical potential, but the cantilever and the pyramid also effect. The closer the tip is to the sample, better the resolution however this effects the electrical potential. Hence, the height of the probe and the area to be tested were kept same throughout the experiment to ensure fair results. The electric potential was studied first by increasing the value of relative humidity from dry to wet conditions for 0%, 25%, 50%, 70% and 100% humidity. The sample was then studied for reverse conditions

i.e. from wet to dry. This was done to ensure the repeatability of the experiment. For each measurement, scan size of 4 μm was considered. Scan ratio was 0.249 Hz and tip velocity was kept at 1.99 $\mu\text{m/s}$. The following steps were carried out to investigate the effect of relative humidity on the sample.

- a. Make a scan upwards for 4 μm area; here we need to specify that scanning in AFM is done line by line, therefore lines of the image are added in the bottom part of the picture and the picture “builds up” with each line of pixels upwards. Scanning upwards may show different results compared to scanning downwards because of sample’s drift. We needed to be sure that all scans were done equally at the same geometrical location on the sample
- b. Make a scan in downwards for the same area to ensure each reading is taking place for the chosen area;
- c. Lift the probe above the sample by 6 μm with the help of z-piezoelectric feature and establish the desired humidity by carefully closing the inlet and outlet of the gas cell once the desired humidity level is achieved (Note: take the bubbler tube out or open an outlet to prevent the buildup of pressure in the setup);
- d. Land the probe and scan the sample but discard the image if it is blur due to presence of dirt or other particles and repeat this step again;
- e. Repeat step c and d for all value of relative humidity from 0% to 100% and then back to 0%.

First the humidity conditions were changed in a controlled manner from dry to wet. The following observations were made for each humidity value over the same 4 μm by 4 μm area:

1. Dry condition:

The dry valve was turned to achieve 410⁰ to establish dry conditions. Dry air was flushed through the sample for 30 minutes and the reading on pc display was constant at 4% which was considered as completely dry (Figure 39 a).

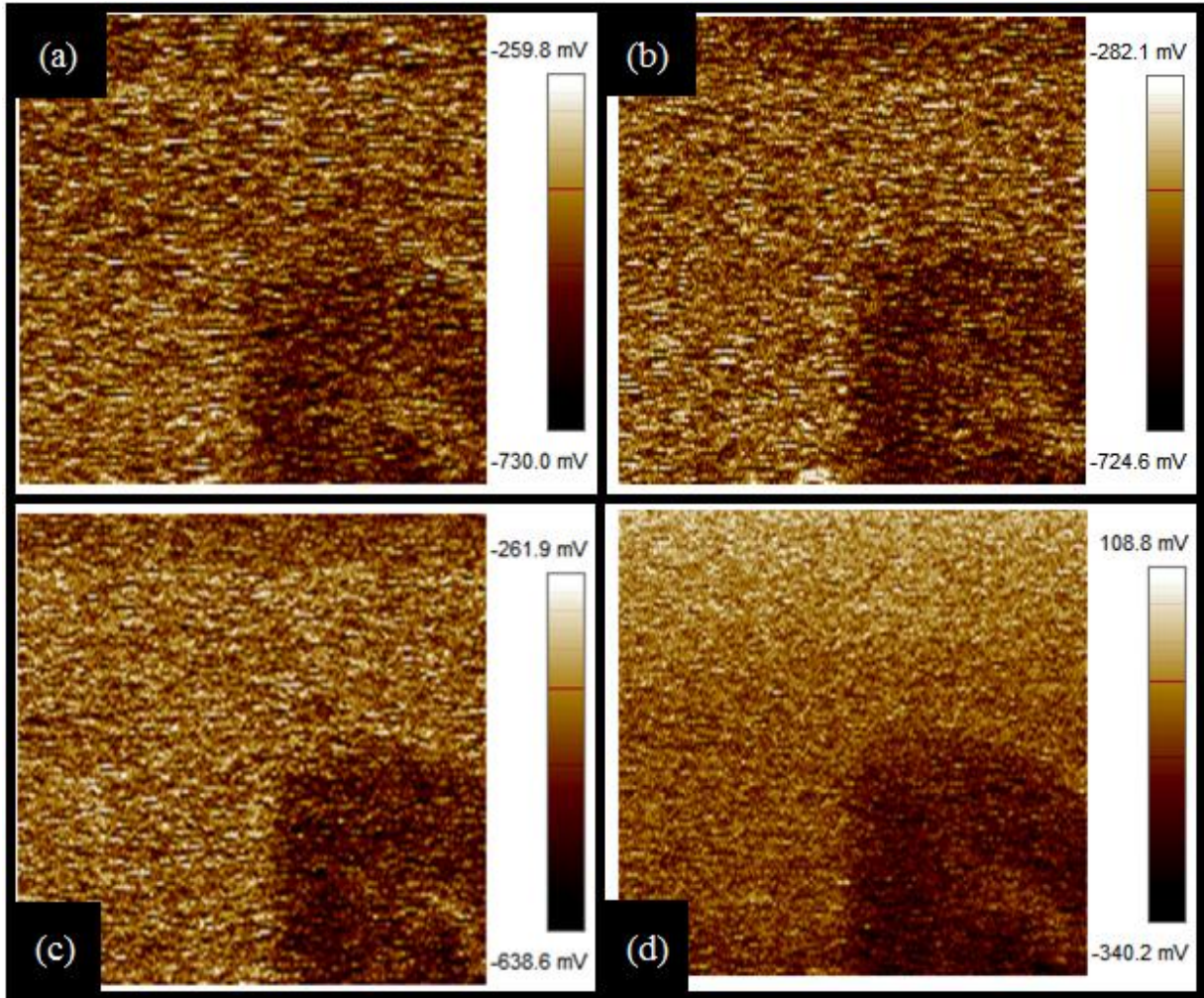


Figure 39: Map of electric potential map (mV) for dry to wet conditions at (a) initial dry conditions, (b) 25 % RH, (c) 50 % RH, (d) and 70 % RH.

25% Relative Humidity:

To obtain 25%, i.e. the room humidity, the dry valve was carefully turned to be 370°. A maximum of 20% was reached after 6 minutes and the system was closed. Throughout the experiment, the RH value remained stable at 20% (Figure 39 b).

2. 50% Relative Humidity:

The angle of dry valve was changed to 330° in order to achieve 50% humidity. A maximum of 46% was reached after 13 minutes which dropped to 43% during the experiment (Figure 39 c).

3. 70% Relative Humidity:

For 70% relative humidity, dry valve's angle was turned to 295° . After waiting for 7 minutes, maximum value of 74% RH was reached which dropped down to 60% during the scan (Figure 39 d).

4. 100% Relative Humidity:

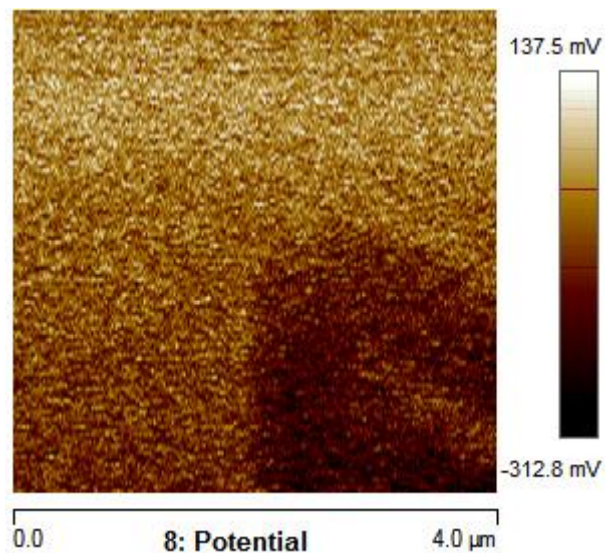


Figure 40: Electric potential map at established 100 % RH.

The dry valve was turned to read 240° to achieve 100%.

Abnormalities occurred when the humidity was increased to 100% as clusters of light spots covered the sample as shown in Figure 41 (a). These light spots are assumed to be water particles due to high humidity value so the system was closed at 94% humidity after waiting for 12 minutes. Condensation of water molecules due to temperature difference may be a possible explanation for this unexpected feature.

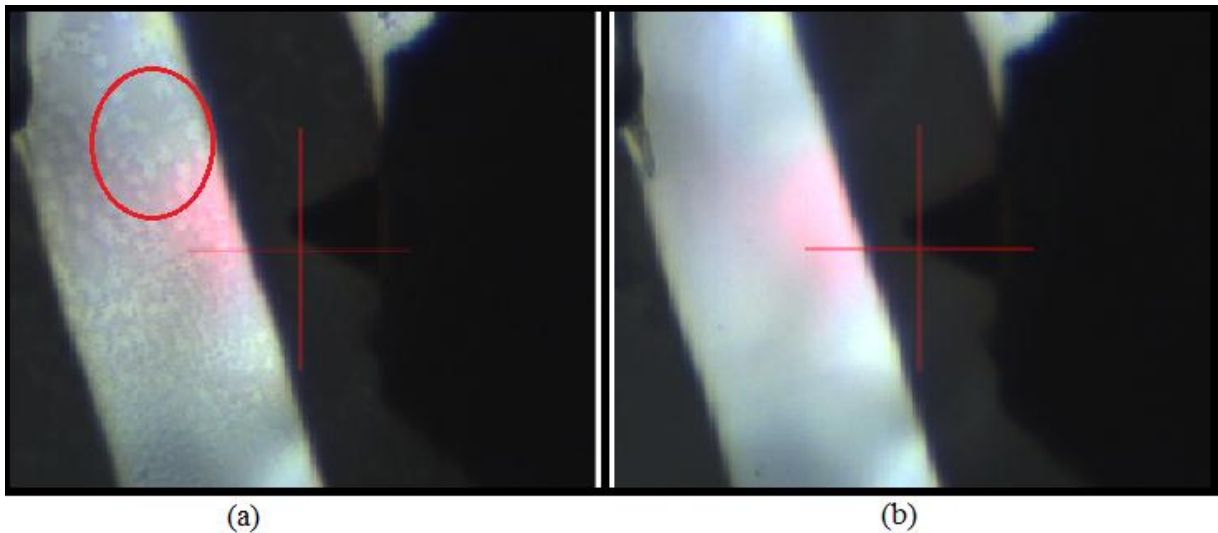


Figure 41: (a) Occurrence of light spots over the sample at 94 % humidity, (b) Water layer disappeared after humidity level was decreased from 94% to 82%.

Another explanation could be the swellings on the surface of sample due to not enough time given for the condition to establish and get stable which was a limitation throughout the experiments because of the fluctuations in the main air source from the university. However, they disappeared when the humidity level was decreased to 82% as shown in Figure 41 (b).

The value of humidity was then decreased from 100% to 0% and the following observations were made at measurement.

1. 100% Relative Humidity

The same value was kept as achieved when going from dry to wet conditions as the experiment was continuous.

2. 70% Relative Humidity

The angle of dry valve was decreased to 70% and a maximum of 65% RH was achieved after 15 minutes. The value of RH stayed constant at (66 ± 2) % during the experiment (Figure 42 a).

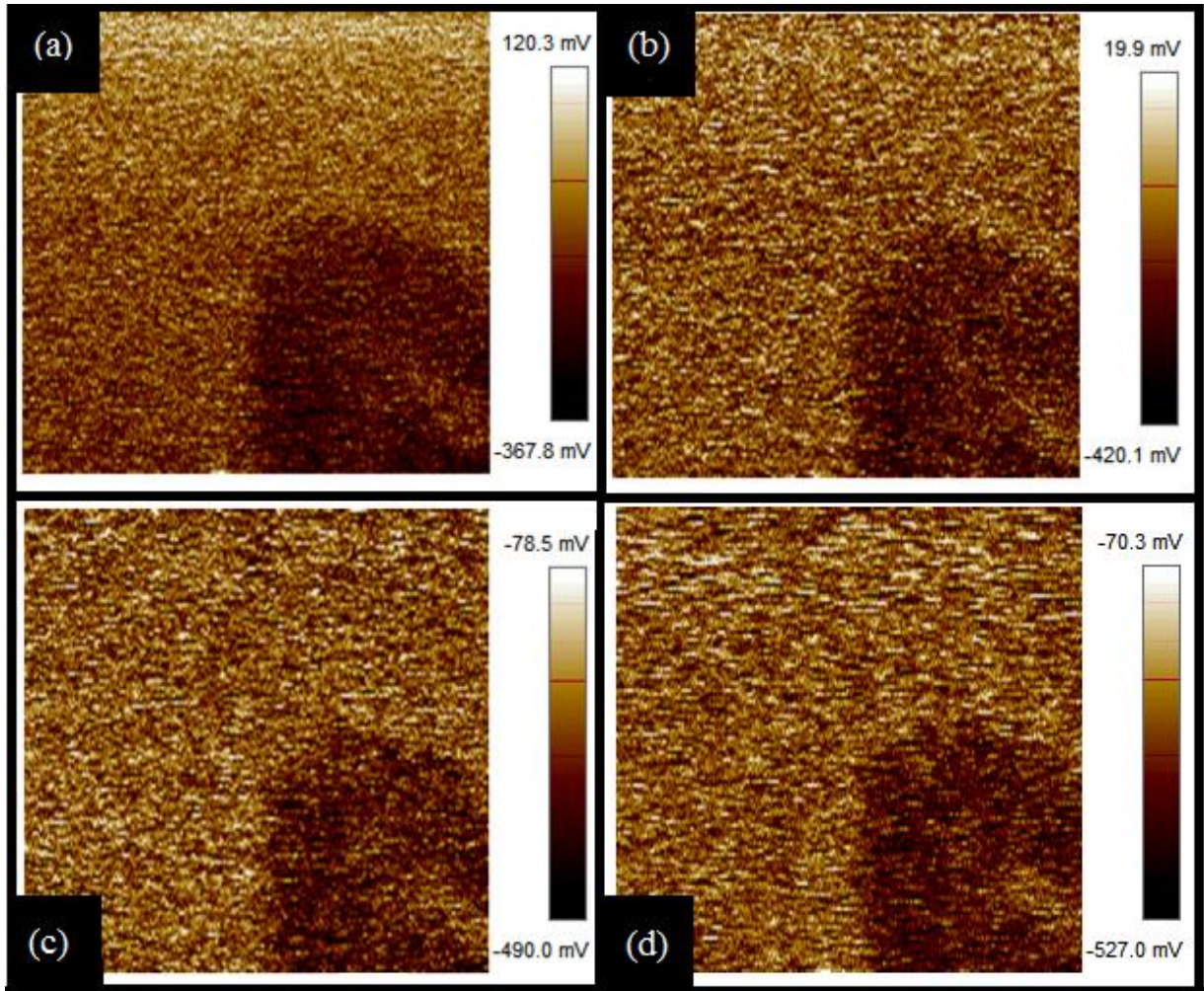


Figure 42: Map of electric potential (mV) for wet to dry conditions at (a) 70 % RH, (b) 50 %, (c) 25 % and (d) dry conditions.

3. 50% Relative Humidity

In order to achieve 50%, the angle of openness of dry valve was decreased to 330°. The value of Relative Humidity stabilized at 50% after 11 minutes and stayed constant at (50 ± 1) % throughout the scan. A darker electric potential was achieved compared to the scan for 70% RH which means a decrease in the value of electric potential (Figure 42 b).

4. 25% Relative Humidity

After decreasing the angle to 370° , the RH value stabilized at 22% after 11 minutes and connections to gas cell were closed to conduct the scan. The value of RH stayed constant at (25 ± 2) % throughout the measurement (Figure 42 c).

Care was taken while decreasing the angle in order to ensure constant bubbling so the sample stays wet. Otherwise, if the bubbling stops, the humidity level changes and the sample is repeatedly charged and discharged and these fluctuations can cause unwanted noise in the electrical potential and may also negatively affect the repeatability of the results.

In order to ensure the continuation of bubbling, the angle was slightly decreased so the sample stays wet, and when equilibrium was reached within the sample, the angle of dry valve was changed back to 370° after 3 minutes.

5. Dry conditions

After decreasing the angle of openness of dry valve to 410° , the RH value stabilized at 5% after waiting for 20 minutes, which is 1% higher than the value of dry air achieved at the beginning of the experiment. During the experiment, the value of RH increased from 5% to 10% and then stayed constant at (8 ± 2) % (Figure 42 d).

This anomaly may be because of less time given for the sample to dry or a faster scan was needed as soon as the humidity value reached 5% instead of waiting for 20 more minutes.

6 Analysis of Results

Values of electric potential for each humidity value were selected from a specific rectangular section (blue region) as shown in the in Figure 43.

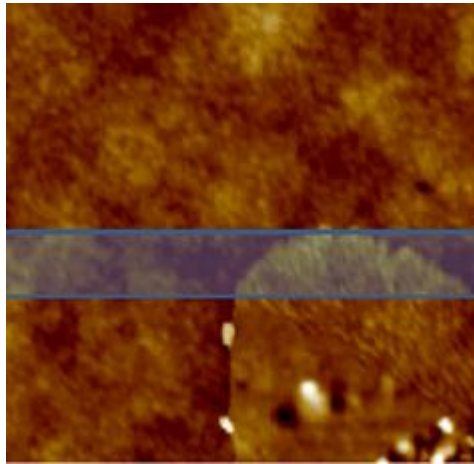


Figure 43: Specific rectangular area selected to obtain electric potential values.

A rectangular block was chosen instead of a line to minimize the error margin due to any background noise by averaging the errors for each point within the rectangular section.

The electric potential values obtained for all humidity values were used to construct a graph as shown in Figure 44. All trend lines were made in the same graph for better comparison.

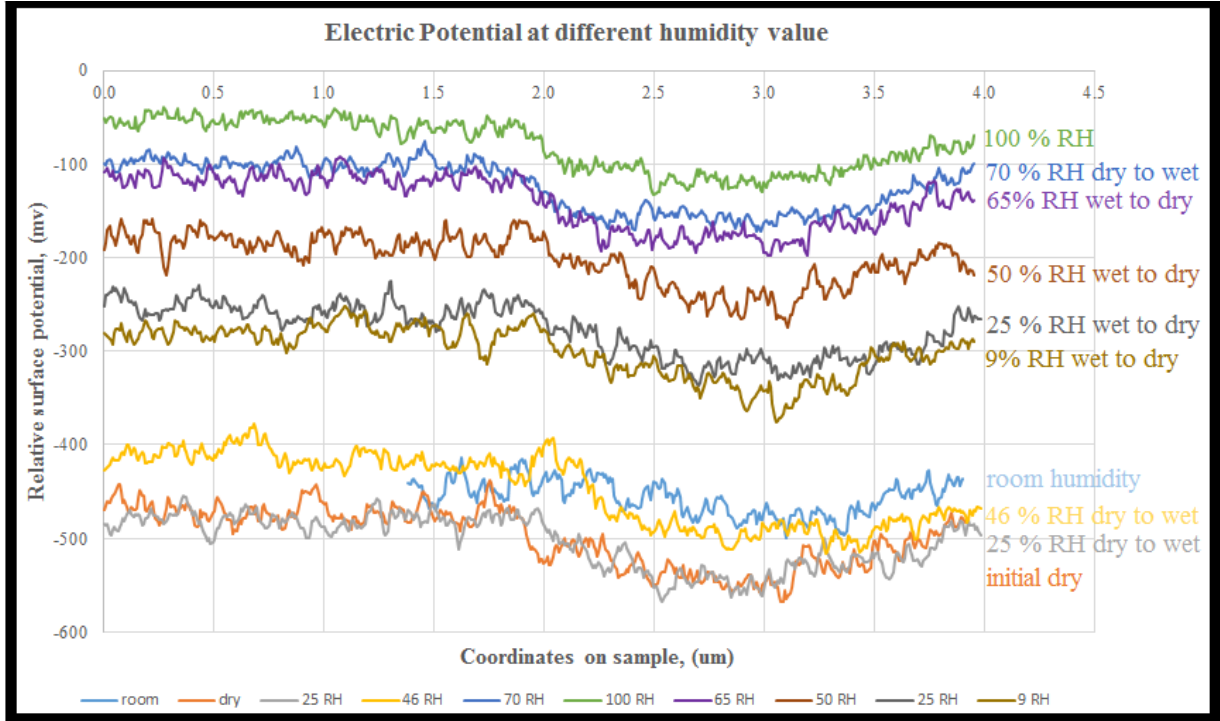


Figure 44: Comparison of electric potential for all established humidity conditions.

According to the graph obtained, variation in electric potential was observed when a change in humidity value was obtained. This was the goal of this experiment. Electric potential values were observed to increase when the value of humidity was increased from dry conditions to wet conditions. The reverse was true when decreasing humidity value from wet to dry which also proved the repeatability of the experiment.

However, in order to predict the relationship between peak electric potential and percentage of humidity, graph was constructed as shown in Figure 45. The graph shows the peaks of all humidity values tested during the experiment, however graph trends are overlapping and it is difficult to see all peaks so few electric potential values are selected to construct Figure 46 to achieve a better comparison.

It is observed from the graph that the peak value of electric potential shifts when the value of relative humidity is changed.

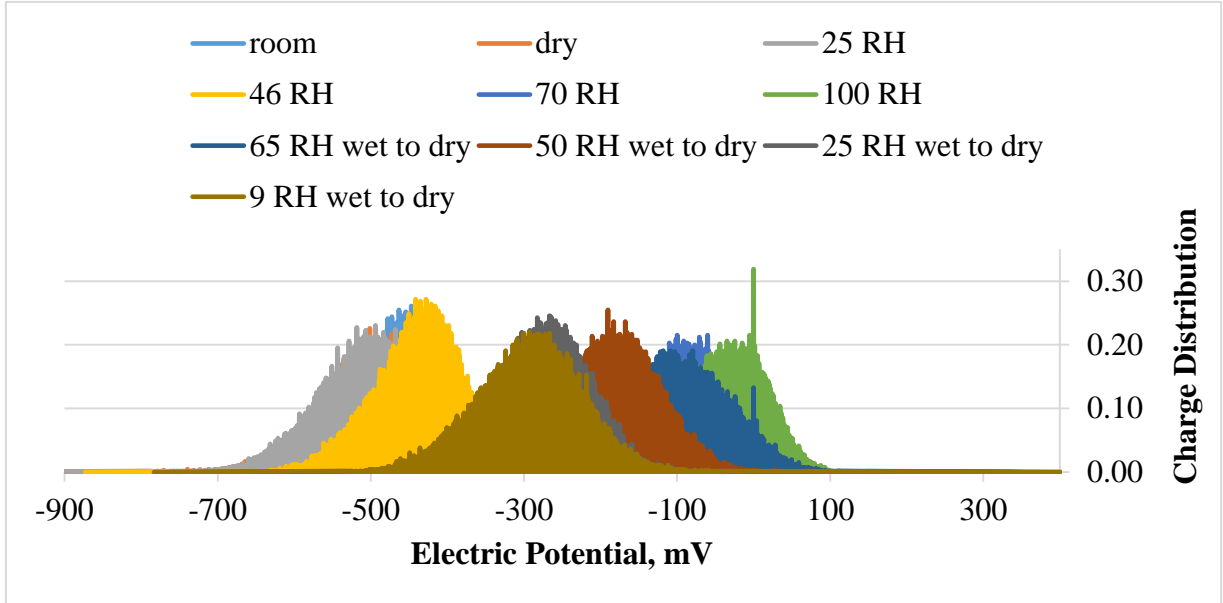


Figure 45: Comparison of peak electric potential at various RH values.

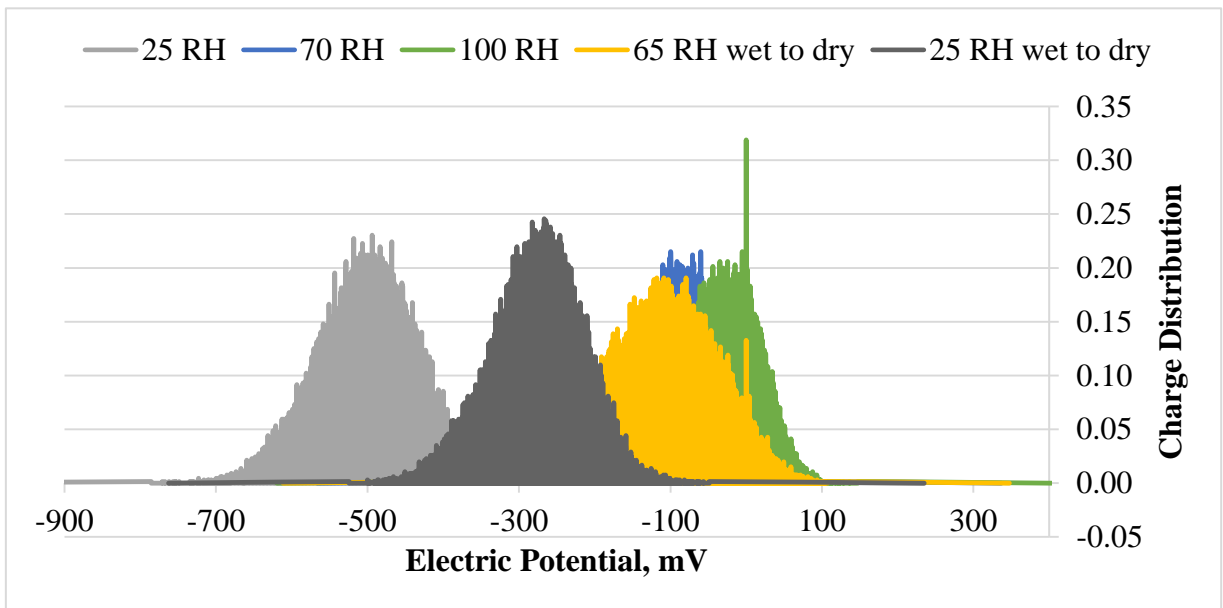


Figure 46: Graph of Charge Distribution vs Electric Potential of selected RH values for clear comparison.

As seen from Figure 45 and Figure 46 when the humidity is increased, the peak shifts towards the right which means the electric potential is increasing and when the value of humidity is

decreased the peak shifts towards the left which signifies a decrease in the value of electric potential.

The graphs show more repeatability at higher humidity values which is evident from the increased overlap in graphs for wet to dry and dry to wet conditions. However, the overlap between curves of lower humidity value is less which indicates lower repeatability. This can be explained by the fact that less time was given to samples to dry and get stable at the desired lower humidity when moving from wet to dry conditions. Hence, there was still some moisture in the sample from previous higher humidity value which was effecting the electric potential achieved at lower humidity.

Another feature visible in the graph above is a spike at 100% humidity which may be because of the saturation of water molecules and the formation of a thin water layer over the surface as explained Chapter 5.

Figure 45 was used to determine the most frequently occurring electric potential achieved for each humidity which was utilized to construct the bar chart in Figure 47.

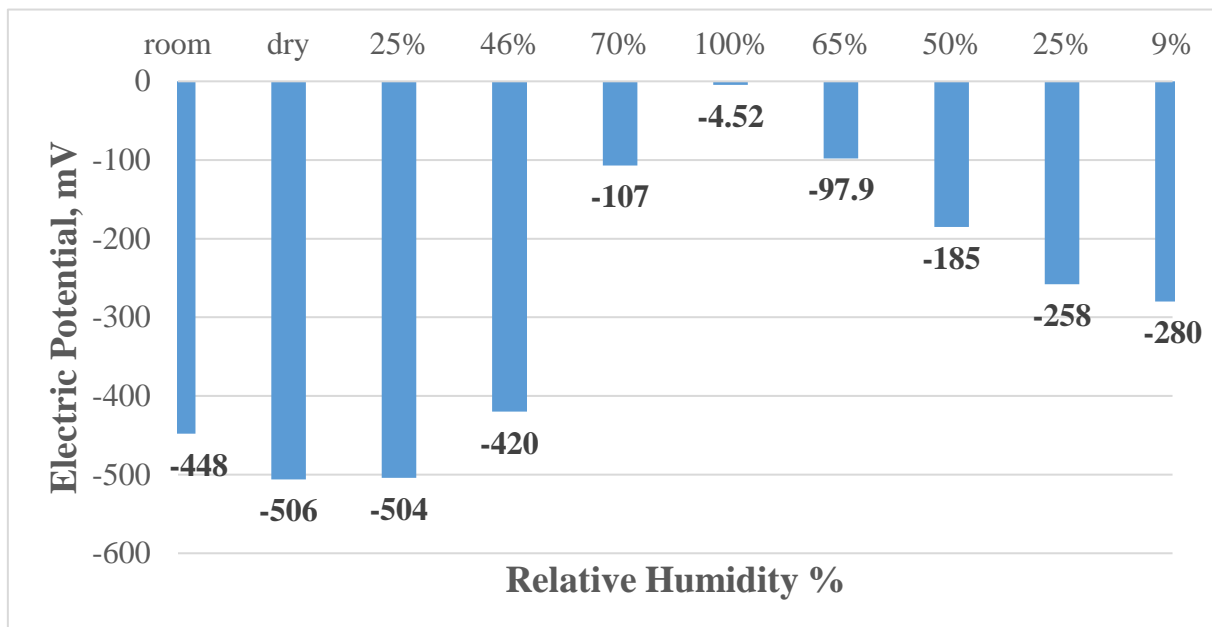


Figure 47: Comparison of most frequent electric potential for each humidity value.

The bar chart shows the mode value of electric potential for each value of humidity where x-axis shows the percentage of RH and y-axis represents the electric potential (mV). Highest value

was achieved for 100% RH at -4.52 mV and lowest mode electric potential achieved for dry conditions at -506 mV. A difference of 502.52 mV electric potential is achieved during the experiment.

The hypothesis tested in this Master's Thesis that electric potential across the sample changes with a change in the value of humidity around the sample is successfully proved. Moreover, it is observed that electric potential and relative humidity values have a direct relation with each other i.e. when one increases the other increases and vice versa.

There were certain limitations during the experiment. The actual potential of the probe was unknown in relation to the sample. This can be checked by performing a scan of a metal test sample for the same conditions. Moreover, less time was given for the sample to reach stability as the main air supply was fluctuating. Also, less time was given to sample while going from wet to dry conditions, so that the sample does not get dry. Due to this, when the closed conditions were established, the stabilized value was more than what was required. The RH value of dry air source from University was measured to be 4% and it was assumed that 4 % is 0 %. However, it is possible that the air was not completely dry but had a constant humidity value of 4 %. The above-mentioned obstacles will be reflected and corrected until the end of the HUNTER project.

Summary

In the course of this Master's work, advances of KPFM technique were learnt and utilized to plan the experiment to examine proof of the concept "hypothesis of humidity-to-electricity conversion". AFM software and hardware for Bruker Multimode 8 station were learnt for conducting experiments and to establish experimental parameters. Furthermore, an experimental setup was designed to perform the KPFM studies in controlled humidity environment. This station was assembled by combining a humidity changing system with a humidity sensing system to both monitor the humidity and organize feedback for steady experimentation. Great care was taken to minimize the interference of atmospheric humidity so the readings were not spoiled by external parameters but reflected the desired experimental conditions set by ourselves. This was a laborious and time consuming task that was solved with the help of improvising available means.

Five various sensors were used to measure relative humidity and temperature accurately; however, it was discovered after variability of their readings that these sensors were incorrectly calibrated and partly flawed. The reference sensor (Vaisala) was established using extreme humidity conditions, i.e. absolutely dry and absolutely humid air. The remaining four sensors were calibrated with respect to Vaisala within their operation ranges. This was done according to the procedure described in detail in section 4.1 of this thesis. However, it was observed that analogous HIH-4040 was the most adequate sensor for our study due to its short response time, ability to work within a wider range of humidity and temperature, and small size suitable for mobile setup. Therefore, only HIH-4040 was used to measure the value of relative humidity throughout our experiments. As a technical result, a custom-built inexpensive humidity control system was combined in laboratory of Solid-state Physics of Lappeenranta University of Technology (LUT) with the help of my supervisor.

This measuring system helped us to perform a repeatable examination of the underlying hypothesis in the H2020 “HUNTER” project, suggesting humidity-to-electricity conversion. During the experimental work of this Master’s thesis, ZrO₂ samples were thoroughly investigated using AFM microscopy and KPFM in particular. The surface topography of the samples, phenomenon of accumulation of electric charge and its influence towards the surface characteristics were studied. As was mentioned earlier, the effect of level of relative humidity on the surface electric potential was studied to reach a conclusion regarding the relationship between percentage of relative humidity of gas environment and the build-up of charge on the surface of a sample placed in it.

It is possible to summarize that the experiment with PMMA-ZrO₂ (Poly methyl methacrylate zirconium) nanocomposite was successful in proving the hypothesis that electric potential of a sample can vary with change in humidity value. The results of this thesis correspond well with the opinion of other researchers such as F. Galembeck, A. Doroshkevich and A. Lyubchyk, whose works were an inspiration for this thesis. **An electric potential difference of ~500 mV between the grounded SPM probe and the sample was observed while changing value of relative humidity of ambient gas environment from 0 % to 100 % inside the closed gas sample. This level of voltage output seems promising for sub-volt device applications and**

proves that zirconia nanoparticles are a suitable candidate for anticipated humidity-to-electricity power device utilizing hygroelectricity principle.

It is possible to note few uninvestigated issues and drawbacks of our measuring approach. It is vital to recognize the possibility of influence of electrical potential due to surface of the SPM probe itself, which may alter the change in electrical potential between the probe and the surface of the sample. The following improvements can be installed in our system coupling the SPM with self-made humidity control setup to further advance SPM measurements in the future. Primarily, fabrication of small samples with size dimensions less than 8 x 8 x 5 mm (length x width x height) is important so the sample can fit inside the gas cell of the Multimode 8 SPM to avoid gas leakages. Moreover, it is necessary to allow electrical contact with two electrodes via isolated metallic microwires to connect grounding and be able to apply bias to the second electrode. Latter is necessary to study the influence of voltage applied between two neighbouring aluminium electrode pads grown by lithography below the PMMA/ ZrO₂ layer. Thirdly, a closed chamber can be built around the microscope to decrease leakages occurring due to high gradient of humidity between imperfectly sealed gas cell and laboratory room air having an average relative humidity of 25 %. It is important to note that we assumed that no loss of electric charge is occurring in the system, which can leave a room to unjustified assumptions of breakage of charge balance. We considered that the charges with opposite electric sign were not lost, but were collected by the grounding, electrodes and partially by the cell walls working as reference electrode as per the principle of Faraday's cage. Furthermore, other types of materials and particle sizes need to be tested apart from ZrO₂ nanoparticles because Al₂O₃, which was tested by our colleges in laboratory of DIPE (Ukraine) has previously shown similar effect of electrification from bulk pressurized pellets of alumina nanopowder. Finally, more attention needs to be paid to application of QNM™ mode of multimode 8 SPM in the study of relationship between humidity and electric potential. Since QNM mode can visualize the map of nano-local adhesion (while adhesion is one of the outcomes of van der Waals force, i.e. electromagnetic interaction), then accumulated electric charge can influence local electrification and adhesion of the surface. This can simplify the SPM experimental concept and thereby needs further attention.

References

- [1] Turner, J.A., 1999. A realizable renewable energy future. *Science*, 285(5428), pp.687-689.
- [2] Shiklomanov, I.A., 2000. Appraisal and assessment of world water resources. *Water international*, 25(1), pp.11-32.
- [3] Williams, J.C., 2006. History of energy. The Franklin institute's resources for science learning scientists of energy.
- [4] Smil, V., 2004. World history and energy. *Encyclopedia of energy*, 6, pp.549-561.
- [5] Horizontal wheels. Tide mill institute [online document]. [Accessed on 16 March 2017]. Available at: <http://www.tidemillinstitute.org/27.html>
- [6] Edgerton, R.H., 1982 Available energy and environmental economics, United States, Lexington Books, Lexington.
- [7] Andrew Stacey, 2011. Energy return on energy invested: The Azimuth project. [online document]. [Accessed on 31 May 2017]. Available at: <http://www.azimuthproject.org/azimuth/show/Energy+return+on+energy+invested>
- [8] Koroneos, C., Spachos, T. and Moussiopoulos, N., 2003. Exergy analysis of renewable energy sources. *Renewable energy*, 28(2), pp.295-310.
- [9] Bahadori, A., Zahedi, G. and Zendehboudi, S., 2013. An overview of Australia's hydropower energy: Status and future prospects. *Renewable and sustainable energy reviews*, 20, pp.565-569.
- [10] Turner, J.A., 1999. A realizable renewable energy future. *Science*, 285(5428), pp.687-689.
- [11] Lewis, N.S., 2007. Toward cost-effective solar energy use. *science*, 315(5813), pp.798-801.

- [12] Mekhilef, S., Saidur, R. and Safari, A., 2011. A review on solar energy use in industries. *Renewable and sustainable energy reviews*, 15(4), pp.1777-1790.
- [13] Tsoutsos, T., Frantzeskaki, N. and Gekas, V., 2005. Environmental impacts from the solar energy technologies. *Energy Policy*, 33(3), pp.289-296.
- [14] Razykov, T.M., Ferekides, C.S., Morel, D., Stefanakos, E., Ullal, H.S. and Upadhyaya, H.M., 2011. Solar photovoltaic electricity: Current status and future prospects. *Solar Energy*, 85(8), pp.1580-1608.
- [15] Abu-Jasser, A., 2010. A stand-alone photovoltaic system, case study: a residence in Gaza. *Journal of applied sciences in environmental sanitation*, 5(1), pp.81-91
- [16] Johansson, T.B., 1993. *Renewable energy: sources for fuels and electricity*. Island press.
- [17] McKendry, P., 2002. Energy production from biomass (part 1): overview of biomass. *Bioresource technology*, 83(1), pp.37-46.
- [18] The benefits of biomass power, 2013. Integro earth fuels, Inc. [online document]. [Accessed on 23 May 2017]. Available at: <http://www.integrofuels.com/sustainability/biomass-benefits/>
- [19] Rehman, S. and Ahmad, A., 2004. Assessment of wind energy potential for coastal locations of the Kingdom of Saudi Arabia. *Energy*, 29(8), pp.1105-1115.
- [20] Akpınar, E.K. and Akpınar, S., 2005. An assessment on seasonal analysis of wind energy characteristics and wind turbine characteristics. *Energy Conversion and Management*, 46(11), pp.1848-1867.
- [21] Kaygusuz, K., 2002. Renewable and sustainable energy use in Turkey: a review. *Renewable and sustainable energy reviews*, 6(4), pp.339-366.
- [22] Chen, Z., Guerrero, J.M. and Blaabjerg, F., 2009. A review of the state of the art of power electronics for wind turbines. *IEEE transactions on power electronics*, 24(8), pp.1859-1875.
- [23] Barbier, E., 2002. Geothermal energy technology and current status: an overview. *Renewable and sustainable energy reviews*, 6(1), pp.3-65.

- [24] Geothermal power plants: Geothermal explained, 2016. U.S. Energy information administration. [online document]. [Accessed on 28 May 2017]. Available at: https://www.eia.gov/energyexplained/index.cfm?page=geothermal_power_plants
- [25] Paish, O., 2002. Small hydro power: technology and current status. *Renewable and sustainable energy reviews*, 6(6), pp.537-556.
- [26] Li, D.H., Cheung, G.H. and Lam, J.C., 2005. Analysis of the operational performance and efficiency characteristic for photovoltaic system in Hong Kong. *Energy conversion and management*, 46(7), pp.1107-1118.
- [27] Ackermann, T. and Söder, 2002. L., An overview of wind energy-status 2002. *Renewable and sustainable energy reviews*, 6(1), pp.67-127.
- [28] Bermann, C., 2007. Impasses and controversies of hydroelectricity. *Estudos avançados*, 21(59), pp.139-153,
- [29] Helman, D.S., 2011. Catching lightning for alternative energy. *Renewable energy*, 36(5), pp.1311-1314.
- [30] Borghetti, A., Nucci, C.A. and Paolone, M., 2003. Effect of tall instrumented towers on the statistical distributions of lightning current parameters and its influence on the power system lightning performance assessment. *International transactions on electrical energy systems*, 13(6), pp.365-372.
- [31] Dwyer, J.R., Uman, M.A., Rassoul, H.K., Al-Dayeh, M., Caraway, L., Jerauld, J., Rakov, V.A., Jordan, D.M., Rambo, K.J., Corbin, V. and Wright, B., 2003. Energetic radiation produced during rocket-triggered lightning. *Science*, 299(5607), pp.694-697.
- [32] Comtois, D., Chien, C.Y., La Fontaine, B., Martin, F., Pepin, H., Johnston, T.W., Kieffer, J.C., Rizk, F.A.M., Vidal, F., Potvin, C. and Couture, P., 2002, May. Triggering of a laser-guided positive leader from a ground rod for the purpose of lightning control. In *Plasma Science, 2002. ICOPS 2002. IEEE conference record-abstracts. The 29th IEEE International conference on* (p. 141). IEEE.

- [33] Rycroft, M.J., Harrison, R.G., Nicoll, K.A. and Mareev, E.A., 2008. An overview of Earth's global electric circuit and atmospheric conductivity. *Space science reviews*, 137(1-4), pp.83-105.
- [34] Costa, M.H. and Foley, J.A., 1998. A comparison of precipitation datasets for the Amazon basin. *Geophysical Research Letters*, 25(2), pp.155-158.
- [35] Chua, K.G., Hor, Y.F. and Lim, H.C., 2016. Raindrop kinetic energy piezoelectric harvesters and relevant interface circuits: Review, issues and outlooks. *Sensors & transducers*, 200(5), p.1.
- [36] Li, H., Tian, C. and Deng, Z.D., 2014. Energy harvesting from low frequency applications using piezoelectric materials. *Applied physics reviews*, 1(4), p.041301.
- [37] Yang, Y., Wang, S., Zhang, Y. and Wang, Z.L., 2012. Pyroelectric nanogenerators for driving wireless sensors. *Nano letters*, 12(12), pp.6408-6413.
- [38] Guigon, R., Chaillout, J.J., Jager, T. and Despesse, G., 2008. Harvesting raindrop energy: theory. *Smart materials and structures*, 17(1), p.015038.
- [39] Shu, Y.C. and Lien, I.C., 2006. Efficiency of energy conversion for a piezoelectric power harvesting system. *Journal of micromechanics and microengineering*, 16(11), p.2429.
- [40] Manak, R., Prabhakar, V. and Saini, J., 2013. Nanomodules-solar energy harvesting devices. *International journal of current engineering and technology*, 3(5), pp.1672-1678.
- [41] Roduner, E., 2006. Size matters: why nanomaterials are different. *Chemical society reviews*, 35(7), pp.583-592.
- [42] Schaller, R.D. and Klimov, V.I., 2006. Non-Poissonian exciton populations in semiconductor nanocrystals via carrier multiplication. *Physical review letters*, 96(9), p.097402.
- [43] O'regan, B. and Grifitzi, M., 1991. A low-cost, high-efficiency solar cell based on dye-sensitized. *nature*, 353(6346), pp.737-740.

- [44] Kymakis, E. and Amaratunga, G.A.J., 2003. Photovoltaic cells based on dye-sensitisation of single-wall carbon nanotubes in a polymer matrix. *Solar energy materials and solar cells*, 80(4), pp.465-472.
- [45] Ducati, T.R., Simoes, L.H. and Galembeck, F., 2010. Charge partitioning at gas– solid interfaces: Humidity causes electricity buildup on metals. *Langmuir*, 26(17), pp.13763-13766,
- [46] McCarty, L.S. and Whitesides, G.M., 2008. Electrostatic charging due to separation of ions at interfaces: contact electrification of ionic electrets. *Angewandte chemie international edition*, 47(12), pp.2188-2207.
- [47] Ovchinnikova, K. and Pollack, 2008. G.HCan water store charge? *Langmuir*, 25(1), pp.542-547.
- [48] Liu, C.Y. and Bard, A.J., 2009. Electrons on dielectrics and contact electrification. *Chemical physics letters*, 480(4), pp.145-156.
- [49] Liu, C.Y. and Bard, A.J., 2010. Electrostatic electrochemistry: Nylon and polyethylene systems. *Chemical physics letters*, 485(1), pp.231-234.
- [50] Rezende, C.A., Gouveia, R.F., 2009. Da Silva, M.A. and Galembeck, F., Detection of charge distributions in insulator surfaces. *Journal of physics: Condensed matter*, 21(26), p.263002.
- [51] Knoll, G.F., 2010. *Radiation detection and measurement*. John Wiley & Sons.
- [52] Naieni, A.K., Bahrami, F., Yasrebi, N. and Rashidian, B., 2009. Design and study of an enhanced Faraday cup detector. *Vacuum*, vol. 83(8), pp.1095-1099.
- [53] Yamamoto, S., Bluhm, H., Andersson, K., Ketteler, G., Ogasawara, H., Salmeron, M. and Nilsson, A., 2008. In situ x-ray photoelectron spectroscopy studies of water on metals and oxides at ambient conditions. *Journal of Physics: Condensed Matter*, 20(18), p.184025.
- [54] Schwarzhinger, G.W., 1992. Outgassing of high-temperature vacuum materials. *Vacuum*, 43(5-7), pp.681-684.

- [55] Weckhuysen, B.M. and Schoonheydt, R.A., 1999. Alkane dehydrogenation over supported chromium oxide catalysts. *Catalysis today*, 51(2), pp.223-232.
- [56] Khaddar-Zine, S., Ghorbel, A. and Naccache, C., 2000. Characterization and catalytic properties of aerogel chromium oxide supported by alumina or silica. *Journal of sol-gel science and technology*, 19(1-3), pp.637-641.
- [57] Hodgson, A. and Haq, S., 2009. Water adsorption and the wetting of metal surfaces. *Surface science reports*, 64(9), pp.381-451.
- [58] Clay, C. and Hodgson, A., 2005. Water and mixed OH/water adsorption at close packed metal surfaces. *Current opinion in solid state and materials science*, 9(1), pp.11-18.
- [59] Gouveia, R.F. and Galembeck, F., 2009. Electrostatic charging of hydrophilic particles due to water adsorption. *Journal of the American chemical society*, 131(32), pp.11381-11386.
- [60] Doroshkevich, A.S., Lyubchyk, A.I., Islamov, A.K., Turchenko, V.A., Glazunova, V.A., Zelenyak, T.Y., Burkhovetskiy, V.V., Shylo, A.V., Balasoiu, M., Saprykina, A.V. and Ohmura, S., 2017, May. Nonequilibrium chemo-electronic conversion of water on the nanosized YSZ: experiment and Molecular Dynamics modelling problem formulation. *Journal of Physics Conference Series*, Vol. 848(1).
- [61] Baikov, P., 2016. Peak Force Kelvin Probe Force Microscopy Investigation of ZrO₂ Nanocomposites for Hygroelectricity Power Element.
- [62] Brownson, D.A. and Banks, C.E., 2010. Graphene electrochemistry: an overview of potential applications. *Analyst*, 135(11), pp.2768-2778.
- [63] Geim, A.K. and Novoselov, K.S., 2007. The rise of graphene. *Nature materials*, 6(3), pp.183-191.
- [64] Soodchomshom, B., 2010. Switching effect in a gapped graphene d-wave superconductor structure. *Physica B: Condensed Matter*, 405(5), pp.1383-1387.
- [65] Heersche, H.B., Jarillo-Herrero, P., Oostinga, J.B., Vandersypen, L.M. and Morpurgo, A.F., 2007. Bipolar supercurrent in graphene. *Nature*, 446(7131), pp.56-59.

- [66] Bolotin, K.I., Sikes, K.J., Jiang, Z., Klima, M., Fudenberg, G., Hone, J., Kim, P. and Stormer, H.L., 2008. Ultrahigh electron mobility in suspended graphene. *Solid state communications*, 146(9), pp.351-355.
- [67] Sato, S., Harada, N., Kondo, D. and Ohfuchi, M., 2010. Graphene—Novel material for nanoelectronics. *Sci Tech*, 46(1), pp.103-110.
- [68] Schmid, G. and Simon, U., 2005. Gold nanoparticles: assembly and electrical properties in 1–3 dimensions. *Chemical communications*, (6), pp.697-710.
- [69] Heath, J.R., Kuekes, P.J., Snider, G.S. and Williams, R.S., 1998. A defect-tolerant computer architecture: Opportunities for nanotechnology. *Science*, 280(5370), pp.1716-1721.
- [70] Balan, L., Malval, J.P., Schneider, R. and Burget, D., 2007. Silver nanoparticles: new synthesis, characterization and photophysical properties. *Materials chemistry and physics*, 104(2), pp.417-421.
- [71] Chen, D., Qiao, X., Qiu, X. and Chen, J., 2009. Synthesis and electrical properties of uniform silver nanoparticles for electronic applications. *Journal of materials science*, 44(4), pp.1076-1081.
- [72] Castro, T., Reifengerger, R., Choi, E. and Andres, R.P., 1990. Size-dependent melting temperature of individual nanometer-sized metallic clusters. *Physical review B*, 42(13), p.8548.
- [73] AZoNano, 2013. Zirconium Oxide Nanoparticles – Properties, Applications [online document]. [Accessed 14 February 2017]. Available at: <http://www.azonano.com/article.aspx?ArticleID=3347>
- [74] Chen, W., Lu, Y.H., Wang, M., Kroner, L., Paul, H., Fecht, H.J., Bednarcik, J., Stahl, K., Zhang, Z.L., Wiedwald, U. and Kaiser, U., 2009. Synthesis, thermal stability and properties of ZnO₂ nanoparticles. *The journal of physical chemistry C*, 113(4), pp.1320-1324.
- [75] Vantomme, A., Yuan, Z.Y. and Su, B.L., 2004. One-pot synthesis of a high-surface-area zirconium oxide material with hierarchically three-length-scaled pore structure. *New journal of chemistry*, 28(9), pp.1083-1085.

- [76] Feynman, R.P., 1960. There's plenty of room at the bottom. *Engineering and science*, 23(5), pp.22-36.
- [77] Binnig, G. and Rohrer, H., 1983. Scanning tunneling microscopy. *Surface science*, 126(1-3), pp.236-244.
- [78] Geydt, P., 2013. Kelvin Probe Force Microscopy (KPFM) characterization of lanthanum lutetium oxide high-k dielectric thin films. Master's thesis, Lappeenranta University of Technology.
- [79] Salapaka, S.M. and Salapaka, M.V., 2008. Scanning probe microscopy. *IEEE control systems*, 28(2), pp.65-83.
- [80] Nonnenmacher, M., o'Boyle, M.P. and Wickramasinghe, H.K., 1991. Kelvin probe force microscopy. *Applied physics letters*, 58(25), pp.2921-2923.
- [81] Melitz, W., Shen, J., Kummel, A.C. and Lee, S., 2011. Kelvin probe force microscopy and its application. *Surface science reports*, 66(1), pp.1-27.
- [82] Glatzel, T., Sadewasser, S. and Lux-Steiner, M.C., 2003. Amplitude or frequency modulation-detection in Kelvin probe force microscopy. *Applied surface science*, 210(1), pp.84-89.
- [83] Pittenger, B., Erina, N. and Su, C., 2010. Quantitative mechanical property mapping at the nanoscale with PeakForce QNM. Application Note Veeco Instruments Inc [online document]. [Accessed on 6 March 2017]. Available at: http://www.cim.unipr.it/html/PeakForce-QNM_AFM_AN128.pdf
- [84] Sweers, K., Van Der Werf, K., Bennink, M. and Subramaniam, V., 2011. Nanomechanical properties of α -synuclein amyloid fibrils: a comparative study by nanoindentation, harmonic force microscopy, and Peakforce QNM. *Nanoscale research letters*, 6(1), p.270.
- [85] Document Revision History: PeakForce QNM User Guide [online document]. [Accessed on 1 May 2017]. Available at: http://www.torontomicrofluidics.ca/cms/manuals/peak_force.pdf

- [86] Preeti Jain, 2012. Humidity sensor, Engineers garage [online document]. [Accessed 18 January 2017]. Available at: <http://www.engineersgarage.com/articles/humidity-sensor>
- [87] Chen, Z. and Lu, C., 2005. Humidity sensors: a review of materials and mechanisms. Sensor letters, 3(4), pp.274-295.
- [88] Humidity sensor theory and behaviour. Honeywell application sheet [online document]. [Accessed on 23 April 2017]. Available at: http://www.hormel.fi/files/7413/5574/9214/Humidity_Sensor_Theory_and_Behavior.pdf
- [89] Two port receive. Arduino Uno [online document]. [Accessed on 12 June 2017]. Available at: <https://www.arduino.cc/en/Tutorial/TwoPortReceive>
- [90] Circuit basics how to set up the DHT11 sensor on an Arduino [online document]. [Accessed 5 March 2017]. Available at: <http://www.circuitbasics.com/how-to-set-up-the-dht11-humidity-sensor-on-an-arduino/>
- [91] How to set up the DHT11 humidity and temperature sensor on an Arduino [online video]. [Accessed 5 March 2017]. Available at: <https://www.youtube.com/watch?v=oZ-oFY6TiPw&t=189s>
- [92] Datasheet for HIH-4000 Series humidity sensor, 2010. Sensing and control honeywell [online document]. [Accessed 20 February 2017]. Available at: <https://sensing.honeywell.com/honeywell-sensing-hih4000-series-product-sheet-009017-5-en.pdf>